THE HYBRID DETECTOR: A PHONON-MEDIATED IZIP STYLE DETECTOR FOR LOW MASS DARK MATTER SEARCH

A Thesis

by

HIMANGSHU NEOG

Submitted to the Office of Graduate and Professional Studies of
Texas A&M University
in partial fulfillment of the requirements for the degree of

DOCTOR OF PHILOSOPHY

Chair of Committee,	Rupak Mahapatra
Co-Chair of Committee,	Nader Mirabolfathi
Committee Members,	Louis E Strigari
	Sunil Chirayath
Head of Department,	G. V. Rogachev

August 2021

Major Subject: Physics

ABSTRACT

There are numerous evidences that support the existence of dark matter but there is no terrestial experiment which has yet been able to detect it. The nature of dark matter is still unknown and multiple candidates are proposed which can be a dark matter particle and can account for the cosmological evidences found till date.

There are multiple earth-based detection experiments like SuperCDMS, LUX etc. which look at the direct interaction of the dark matter particles with some standard model particle. Two big challenges faced by these type of experiments are the low energy threshold of the detectors to reach an energy range where they might be able to detect the dark matter signal and the ability to discriminate signal-like events from the plethora of background events in the detectors due to a variety of other sources.

SuperCDMS interleaved Z-sensitive Ionization and Phonon(iZIP) detectors have shown great success in discriminating electron recoils (the major background) and nuclear recoils (the signal-like events), while the High Voltage (HV) detectors have reached very low (a few eV) energy thresholds by sacrificing that discrimination. This thesis focuses on a novel phonon-mediated two-stage silicon detector that retains both an excellent threshold performance of the HV detector and maintain the iZIP-style background discrimination. Over multiple runs in the Nader's Test Facility and the MINER experiment at NSC, the detector characterization and testing was done with the first prototype Si detector which gave an encouraging result of clear discrimination between signal and background events. This new detector technology has the potential to significantly enhance the sensitivity to dark matter and coherent neutrino scattering experiments beyond the capabilities of current technologies that have limited discrimination at low energies.

ACKNOWLEDGMENTS

First and foremost, I would like to thank my graduate advisor, Dr. Rupak Mahapatra, whose guidance and support helped me to find my way during difficult times in the project. He has been a constant source of encouragement for me during my graduate career.

I would also like to thank Mark Platt, our lab specialist in semi-conductor fabrication and handling whose problem-solving skills has helped me and our group to sail through the engineering problems we face everyday. I am indebted to him for fabricating the first hybrid detector and made this dissertation possible.

I would like to thank our ex-post-doc, Andy Kubik from whom I have learned data analysis starting from the beginner level. His valuable advise and suggestions have helped me immensely during my data analysis of this new detector.

I'd like to say thanks to Andrew Jastram for helping with setting up the detector towers and leading the fridge runs. I am also thankful to other graduate students of our group: Hao Chen, Shubham Verma and Sandro Maludze with whom I have interacted and discussed the different physics concepts which helped me to understand them more clearly.

Finally, I am thankful to Anika Sharma, Murphy and my parents for the selfless love and support during my graduate years.

TABLE OF CONTENTS

Page

LIST OF FIGURES

FIGURE Page

1. INTRODUCTION

Mankind in general, scientific minds in particular, are always fascinated by the unknown and our universe is a box overloaded with it. To set the tone of this chapter, let me ask you(the reader) what would you do if you know there is a big chuck of fine cheese in your house, but the only way you can grab it is to find it first? (Ofcourse, we will find it!) Our current understanding of Dark matter is in a similar situation. There are ample evidences of the existence of dark matter with the added fact that they are much more abundant than normal matter, but there are null results of detection till date. I will walk you through some of the observational evidences found by our cosmology and astrophysics community and discuss one particular experiment, SuperCDMS, which is leading the world in the search for dark matter, which will pave the way towards the crux of this thesis.

1.1 Current understanding of Dark Matter

The composition of the universe is shown in Figure 1.1, interpreted from the data taken by the Planck experiment. The matter around us constitutes only the tiny 4.9% in the diagram. Multiple observations point to the existence of the second big chunk of 26.8% called "dark matter" and the rest is something called "Dark Energy" which we know nothing about.

The curiosity about dark matter grew rapidly after the observation of velocity dispersion of galaxies in the Coma cluster made by Fritz Zwicky in 1933. He ingenously used basic physics effects like Doppler shift and the famous virial theorem to infer a mass-to-light ratio to be a few hundred which though numerically inaccurate, concluded that galaxies are dark matter dominated. Until now, there are various observations ranging in a wide scale of space and time that supports the dark matter hypothesis some of which are briefly discussed below.

1.1.1 Observational Evidences

Most of the observational evidence of dark matter comes from its gravitational interaction with visible matter around it, starting at the smallest scale of dwarf galaxies. These are galaxies with

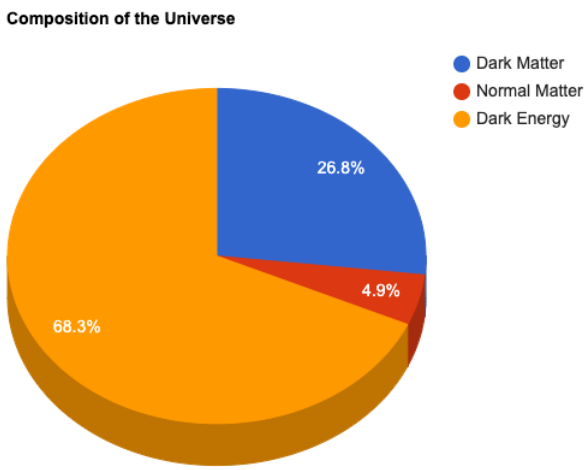

Figure 1.1: Composition of our Universe from measurements by Planck experiment [1, 2, 3]

baryons in diffuse form which make them highly concentrated dark matter objects as compared to other galaxies. The velocities of the few stars in such galaxies have been studied by surveys like Sloan Digital Sky Survey(SDSS) and the mass-to-light ratios are found to be typically 100 times that of other spiral and elliptical galaxies.

Spiral galaxies are larger than dwarf galaxies in the distance scale and consist of a central bulge of stars with younger stars surrounding them in form of a rotating disk. Measurements of the rotation speeds of these galaxies have been done using techniques like Doppler shift in spectral lines, 21 cm HI line etc. As we see in Figure 1.2, the observed rotation curves are flat at higher radii which contradicts our expectation of the orbital velocity of the galactic materials to have a $r^{-1/2}$ behavior at higher radii. Although this is consistent if we assume a roughly spherically-symmetric distribution of the total mass which suggest that matter is extended beyond the edge of the visible disk.

Another larger structure in our universe is galaxy clusters which represent an average composition of matter in a relatively larger region of space. Most of the galaxy clusters are studied using gravitational lensing effects on light rays coming beyond the cluster and x-ray emissions of the hot gas trapped in the cluster itself. One dramatic example is the observation of the "Bullet

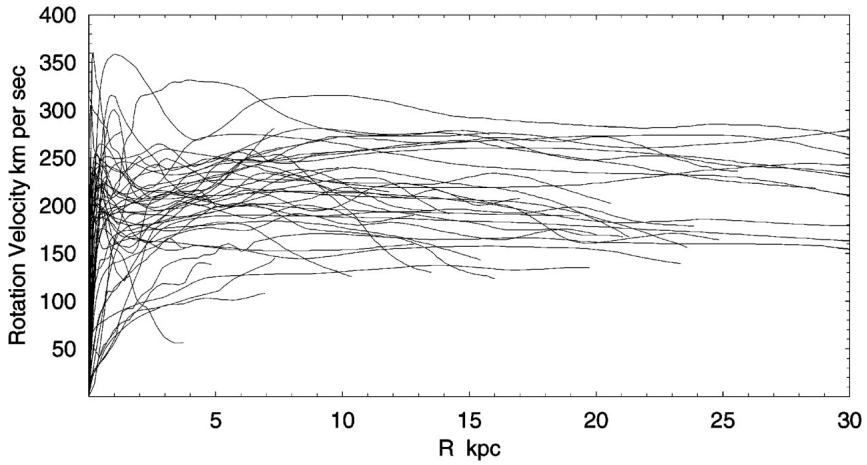

Figure 1.2: Rotational curves for different spiral galaxies, taken from [4]

cluster" where a pair of colliding clusters are visible just after their first collision. This observation confirms that the bulk of the cluster's mass is collision-less which is consistent with properties for dark matter halos.

There are various other observations and theories like large-scale structure formation and Big-band Nucleosynthesis(BBN) which provide experimentally measured quantities like matter densities of cold dark matter(Ω_c) and baryonic matter(Ω_b). One of the most recent and precise measurement is the Cosmic Microwave Background(CMB) measurement by Planck experiment (2013) where the polarization fields and intensity of the CMB photons coming from the recombination era(later epoch than BBN) is measured. After the Big-bang, universe cooled and expanded enough that radiation started streaming freely and these photons carried the information of anisotropies in structures present at that time. These red-shifted photons in the microwave band was found to have a blackbody radiation temperature of 2.7 K with anisotropies ± 0.57 mK. In Figure 1.3 , the power spectra of the CMB is shown as measured by various experiments. The ratio of the first two peaks is related to baryon density while the third peak in relation to the previous ones give information of the dark matter density and the best fit values to the ΛCDM model indicates a dark-matter density of 26.8%[3].

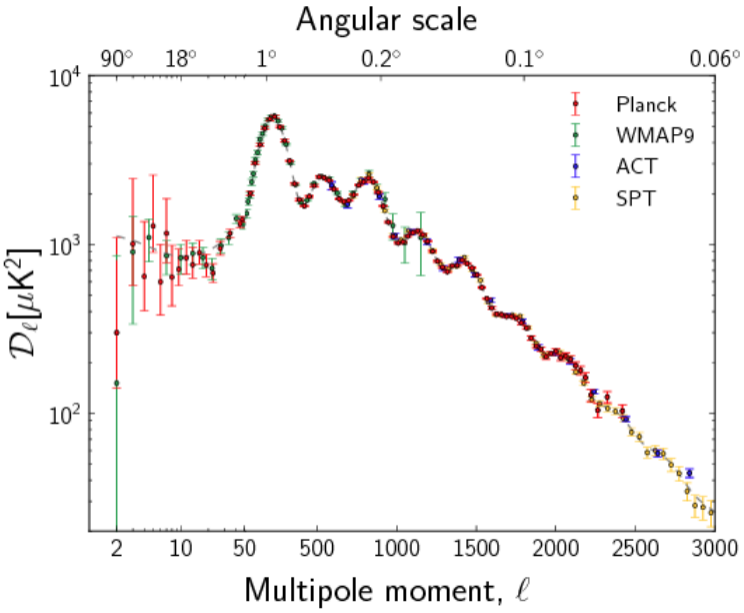

Figure 1.3: Power spectrum of CMB merged from different experiments showing consistency in measured dark matter density parameter for the ΛCDM model from Ref. [3]

1.1.2 Properties and possible candidates for Dark Matter

Based on the results from various observations as noted in Section 1.1.1, we can list down some of the properties of Dark Matter which should hold true as given below:

1. It is massive in comparison to baryonic matter and will hardly interact(weak interactions) with normal matter.

2. It is stable over time. Both cosmological observations(like BAO [7], CMB) and astrophysical measurements(like galactic rotational curves, mass-to-light ratio for dwarf galaxies) have results which agree on the amount of dark matter composition. Since these two types of observations are comparing data from different time scale of the universe, the dark matter particles are stable over billions of years.

3. It is non-relativistic and collisionless. Formation of both large dark matter halos and small scale gravitationally bounded structures are only possible for non-relativistic particles which

hardly collide to itself or other particles. It should be mentioned here that the BAO [7] peak measured at 100 Mpc by the BOSS experiment necessitate the slow-moving nature of dark matter.

4. It should rarely dissipate energy as the dark matter halos seem to be more symmetric and doesn't collapse to form shapes like disks or nebulae like baryonic matter

There are multiple candidates in theoretical physics which satisfies the properties listed above. The most promising out of them is the Weakly Interacting Massive particle(WIMP). These are a generic class of candidates for dark matter in the mass range of 10 GeV to 10 TeV scale. They can weakly interact with baryonic matter and their existence can be derived independently from observations of cosmology as well as requirement of new particles to exist at the weak scale from a particle physics perspective. There are other possible candidates of dark matter like axions, neutralinos etc. details of which can found in Refs [8, 9, 10]

There are three possible ways to search for WIMPs as a dark matter candidate: Indirect detection, Collider production and direct detection. Out of these, I will concentrate my efforts in the direct detection technique.

1.1.3 Direct Detection of Dark Matter

Dark matter can be detected on the Earth by looking at its signature in terrestial detectors. Since WIMP dark matter is neutral and massive, we would expect it to interact weakly to the detectors mostly by scattering off of the nuclei of the detector material. Assuming elastic scattering scenario, the recoil of the nucleus(E_R) due to this particle interaction can be calculated as

$$E_R = \frac{m_\chi v^2}{2} \frac{2m_N/m_\chi}{(1 + m_N/m_\chi)^2} \tag{1.1}$$

Here we have assumed the mass of the nuclei in the detector as m_N and mass of dark matter particle m_χ moving with velocity v. Note that I have averaged over the scattering angle θ to show that the recoil energy is simply a product of the kinetic energy of the WIMP particle and the ratio of the

nuclei over WIMP mass.

The velocity v term in the above expression will not be a constant number, but a distribution based on some model. As a standard practice, a standard halo model described by Lewin and Smith [11] is used which assumes an isotopic Maxwellian WIMP velocity function ($f(v) = e^{-v^2/{v_0}^2}$) with a galactic rotation velocity $v_0 = 230$ km/s and an escape velocity from Earth of 650 km/s. The density of dark matter halo is taken to be $\rho = 0.3$ GeV/c^2/cm^3 around Earth and the Earth's net velocity to be $v_E = 244$ km/s with a small sinusoidal variation term which is neglected. The expected recoil spectrum will take the final form(from [11])

$$\frac{dR}{dE_R} = \frac{R_0}{rE_0} exp(-E_R/E_0 r) \tag{1.2}$$

where E_0 is the most probable incident kinetic energy(from the most probable velocity of the assumed distribution), r is a kinematic factor of the form $4m_\chi m_N/(m_\chi + m_N)^2$, R is the observed event rate per unit mass while R_0 is the total event rate. Given the WIMP mass range, the expected recoil energy range will be 1-100 keV which is achievable with low threshold detectors.

1.2 The SuperCDMS experiment and its detectors

The SuperCDMS experiment is one of the two direct dark matter search experiments funded by the US Department of Energy(DOE), located at an underground mine in Vermilion Range, Minnesota. The underground location with a rock overburden of 714 m aptly reduces cosmic rays and muon flux, which forms a major part of the background in this kind of experiment, where the background rates are multiple orders of magnitude higher than the expected signal. The experiment uses semi-conductor detectors called interleaved Z-sensitive Ionization and phonon detectors(iZIPs) and High Voltage(HV) detectors to discern the remaining background events from the signal events and to detect low threshold signals respectively. These detectors are essentially ultra-pure germanium crystal cylinders of mass approx. 0.6 kg, with sensor material(aluminum and tungsten) photolithographically patterned on the top and/or bottom surfaces. We will discuss the physics of these detectors in the next section which will be heavily used in the follow-up sections.

1.2.1 Detector Crystal Physics

When a high energy particle enters the detector volume and interacts with it, there will be liberation of charges(electron and holes) and lattice vibrations(phonons) inside the crystal. Considering the semi-conductor band gap between valence and conduction bands (E_g), the average energy(ϵ_γ) to produce electron-hole pairs can be parameterized by the band gap energy, kinetic energy of the electrons produced and emitted Raman phonon energy. If the deposited energy in the crystal is E_R, the number of electron and holes generated will be given by $N_{e/h}(E_R) = Y(E_R)\frac{E_R}{\epsilon_\gamma}$ where Y(E_R) is a fractional number(called yield) which takes care of the inefficiency of charge production for nuclear recoils. In Ref [12], a thorough discussion on this factor in terms of stopping power is presented and is parameterized as

$$Y(E_R) = \frac{kg(E_R)}{1 + kg(E_R)} \tag{1.3}$$

where k is a parameter which describe the complexities of the electronic stopping power($k_{Si} = 0.146$, $k_{Ge} = 0.157$) and $g(E_R) = 3{E_R}^{0.15} + 0.7{E_R}^{0.6} + E_R$. Please note that this formula becomes invalid as we approach the energy threshold range to create electrons and nuclei(approx. eV scale). In iZIP detector, the yield is equivalently the ratio of ionization energy to the true recoil energy for a given interaction.

The phonons produced during the interaction are initially out of equilibrium(called athermal phonons) and propagate diffusively inside the crystal. These primary recoil phonons are highly energetic and loose their energy by scattering processes due to mass anisotropies across the crystal lattice and anharmonic decay process where one high energy phonon splits into two lower energy phonons. After multiple downconversions, the phonons can propagate ballistically with a mean free path of approx. 1 cm which is the characteristic length of the crystals. There are essentially three types of phonons produced during an interaction as listed below:

1. Primary recoiling phonons emitted due to electron/hole transition from valence band to conduction bands (in case of both electron and nuclear recoils) and physical displacement of the

nuclei(in case of nuclear recoils only). The energy of the primary phonons is thus, proportional to the total energy deposited in the crystal by the incoming particle.

2. Luke phonons produced by the drifted charge pairs, first reported by Luke, Neganov and Torfimov [13, 14]. In case of an applied electric field across the crystal, the accelerated electron-hole pairs scatter off of lattice sites and the work done in drifting them is emitted as luke phonons with energy(E_L) proportional to the applied voltage(V_b)

$$E_L = \frac{eE_R V_b}{\epsilon_\gamma} \tag{1.4}$$

where e is the electronic unit of charge(in Coulomb) and other terms are previously defined.

3. Relaxation phonons which are released when excited charges relax to the Fermi-sea near the outer edges of the detector in the process of down-conversion. There are multiple mechanisms for relaxation due to factors like deformities in the detector surface, material deposits on the surface etc which has been discussed in detail in Ref. [15]

If we ignore the energy lost due to trapping of charges in the crystal bulk and/or surface losses, the total deposited energy in the crystal can be given by

$$E_{Total} = E_R + Y(E_R)\frac{eV_b E_R}{\epsilon_\gamma} \tag{1.5}$$

1.2.2 Detector Sensor Physics

In the event of an external particle scattering off in the detector volume, there will be a high-density cloud of recoiling phonons and ionized electron-hole pairs. In iZIP detectors, the deposited charge energy is measured with electrode lines deposited and etched on the detector surfaces. The ionized charges from interaction are pulled towards the electrodes by the applied bias voltage where they get trapped by the interleaved potential geometry. These electrodes are divided into two regions: inner and outer to provide a handle to selectively remove events at high radii based on

the charge signal amplitude of the electrodes and the charge readout from the two surfaces of the detector is used to throw away near surface events. The electronic circuit for the charge readout is shown in Fig 1.4, where the detector plays the role of a capacitor(C_d). The image charges on the charge electrode due to movement of charges inside the crystal generates a time-dependent current in the bias resistor which will be readout by the coupling capacitor(C_C) and amplified by a field-effect transistor(JFET) in a low-pass filter configuration.

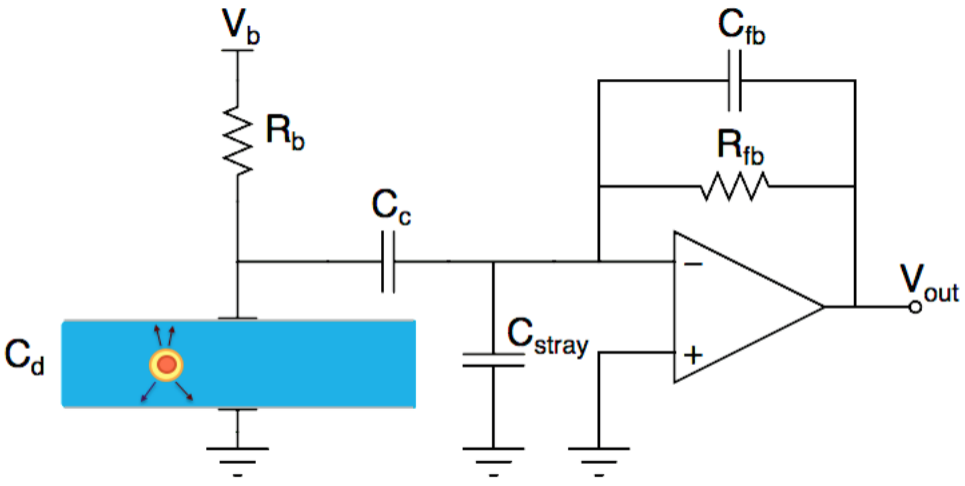

Figure 1.4: Charge readout circuit for an iZIP detector [5]

The athermal phonons produced in the crystal are collected(and measured) in both the iZIP and HV detectors with the help of Quasiparticle-trap-assisted Electrothermal-feedback (QET)Transition Edge Sensors(TESs) lithographed by photographic techniques on the surfaces of the detectors. QETs are aluminum(Al) collector fins with a line-shaped structure of tungsten(W) at the center with some overlapping region in between the two materials. The choice of material is based mainly on the superconducting transition temperatures of Al($T_C = 1.18$ K) and W($T_C = 0.08$ K), and cooper-pair bonding energies($2\Delta_{Al} = 340\mu e$V, $2\Delta_W = 20\mu e$V). As shown in Fig 1.5, when phonons reach the detector surface, they break the cooper-pairs of superconducting Al and produce Bogoliubov quasiparticles which further diffuse into the W layer and get trapped due to

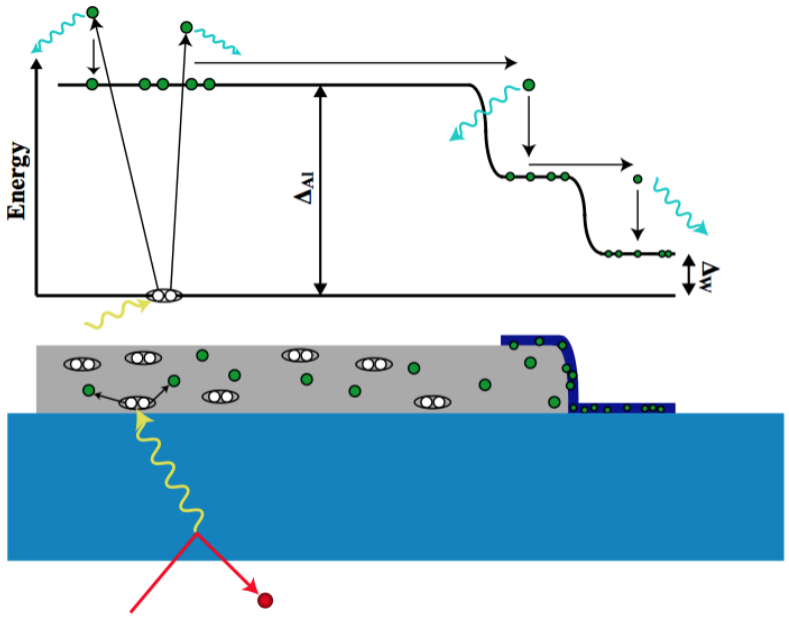

Figure 1.5: Schematic diagram to illustrate phonon signal generation in QETs [5]. Phonons reach the semiconductor crystal(blue) surface to break cooper pairs in Al(gray) to produce quasiparticles which diffuse to W(dark blue)

lower pair-breaking energy of W. This trapping of quasiparticles effectively heat up the TES to raise its resistance sharply which provide an accurate measurement of the deposited energy in the phonon system.

For normal operation of the TESs to respond to every particle interaction, the TESs are held at voltage biased mode which causes Joule heating in the TES according to $P_J = V^2/R$. The heating up of the TESs due to quasiparticle trapping will lead to an increase in resistance of the TES (and a drop in Joule heating) which helps to cool back down the TES to a quiescent state and this mechanism is known as Electro-Thermal Feedback(ETF). The electronic circuit to voltage bias the TES and readout the phonon signal is shown in Figure 1.6. The TES is kept in series connection to an inductor and this circuit is in parallel to a shunt resistor R_{sh}. The change in current due to ETF will cause a change in flux in the coupling inductor(L_i) which is sensed by the SQUID-amplifier circuit. The amplifier output(V_{out}) changes such that the current through the feedback inductor(L_{fb}) neutralizes the flux change in the SQUID. The coil ratio between the two

inductor coils L_i/L_{fb} further enhance the signal by a factor of 10(since the ratio is 10:1) Multiple

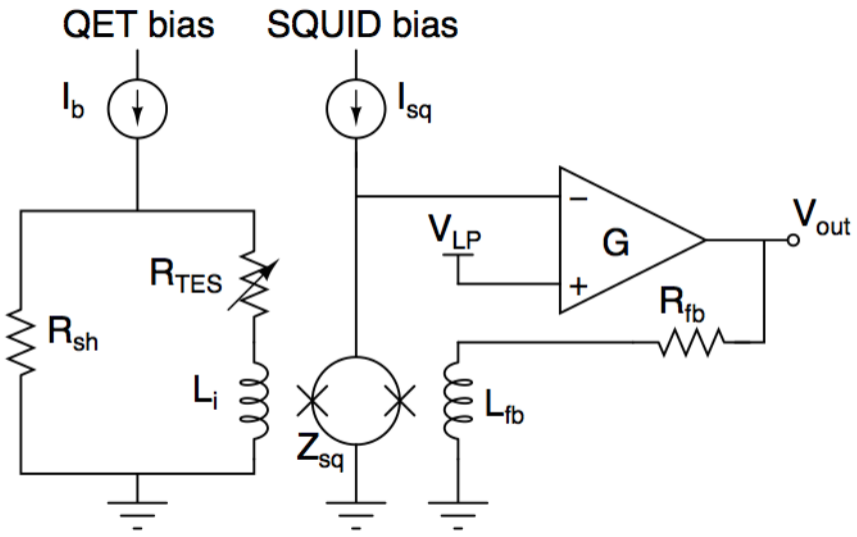

Figure 1.6: Electronic circuit to illustrate phonon signal readout from the TES sensors [6].

TES sensors are bundled up in parallel to form phonon channels and arranged on the detector surfaces in different designs(for example the mercedes (three-pronged star in a circle) design for iZIPs) with the aim to extract information such as energy resolution, event position, etc.

1.3 Limitations in SuperCDMS detectors

There are inherent limitations in the detectors used by the SuperCDMS collaboration which is an active area of R&D. Though iZIP detectors can discriminate electron recoils from nuclear recoils to search for WIMP-like events, the charge readout circuit is noise limited. Though there are multiple sources of noise, the total noise in the charge circuit is dominated by Johnson noise and voltage noise from the JFET amplifiers. For a rough estimate, the total average charge noise is found to be approx. 100 nV/ $\sqrt{Hz}$ which will bury a standard charge pulse with an exponential fall-time of $40\mu s$ and amplitude below 5 keV. This limits the discrimination ability for low energy recoils where the typical energies are in the sub-keV range.

The HV detectors have been designed to mitigate the above issue of noise limitation by using phonon circuit which typically has low noise profile(approx. 15 pA/$\sqrt{Hz}$), but they give up on discrimination power between the type of energy recoils. There are multiple sources of background in the experiment which can mimic a WIMP-like signal in the detectors. Out of them, the most dangerous background are radon/uranium decays(these radioactive atoms cannot be get rid of totally) nearby or inside the detectors. These decays produce nuclear recoils from emission of an α particle or electron recoils [16]. Although extensive efforts have been made to reduce radon contamination levels at various stages of detector fabrication and handling, it would need extensive sophisticated simulation and analysis techniques to estimate their rate to put any dark matter limit based on the results from the experiment. So, it is highly desirable to have discrimination ability at lower energy nuclear recoils to distinguish the background from the dark matter particle interaction signal.

2. HYBRID DETECTOR DESIGN

In the previous chapter, we discussed the limitations of SuperCDMS detectors. In this chapter, I will describe the rationale behind a two stage detector and how it can inherently get over the limitations as those of SuperCDMS detectors. Section 2.2 describes the electric field simulation of the detector geometry and its optimization both in terms of fiducialization and fabrication. I will briefly describe the steps for fabricating the hybrid detector in Section 2.3 and a possibly QET mask design for the phonon sensors in Section 2.4.

2.1 Detector Concept

As mentioned in the previous chapter, the impedence noise during readout for ionization signal in iZIP detectors limits their discrimination ability below 1 keV or so [17]. Since this noise is directly related to the capacitance used in the charge circuit, a possible alternative will be to use SQUID amplifiers in the readout electronics. Since SQUID amplifiers are already used in the phonon circuit, it makes sense to switch to a phonon readout signal instead of charge readout. This idea is used in the CDMS HV detectors to read only phonon signals to achieve world leading noise performance and limits. But in doing so, HV detectors have to give up on discrimination between electron recoils and nuclear recoils which limits their ability for low-threshold background discrimination. The idea of a hybrid two stage detector came up from these two inherent limitations of the SuperCDMS detector technology. By dividing the detector crystal into two regions, recoil phonons and voltage-amplified luke phonons can be readout with phonon sensors independently in the two regions and provides a possibility to maintain discrimination with phonon-only readout electronics.

2.1.1 Physics Model for Hybrid Detector

The hybrid detector has two regions, high voltage region(HV) and low voltage region(LV) connected through a neck as shown in Figure 2.1 and an electric field is maintained across these two regions.

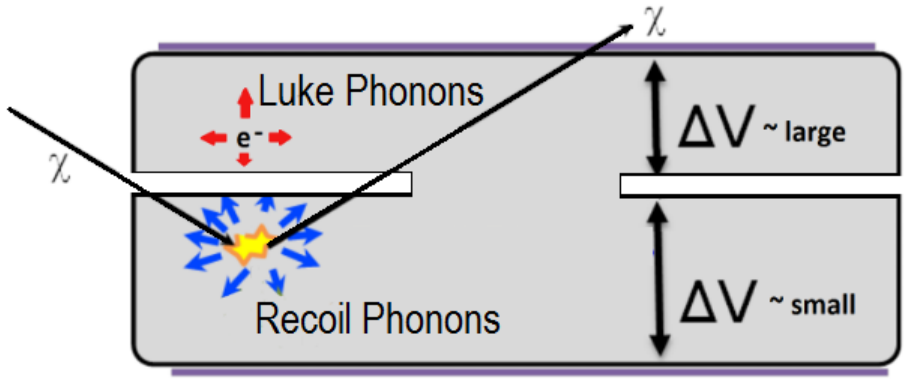

Figure 2.1: Schematic Diagram of a hybrid two-stage detector connected through a neck region.

The LV region constitutes the fiducial volume for signal detection and the HV region mediates the amplification of the NTL phonons due to transport of the charges from the LV region through the neck region. During an interaction in the LV region, the deposited energy will be released in the form of e-h pairs and recoil phonons. These recoil phonons will be collected in the phonon sensors in the LV side(P_{LV}). The e-h pair will drift due to the applied electric field to the HV region through the neck region. Since the HV region has higher voltage drop, the e-h pairs will produce Luke phonons which will constitute our signal on the HV side (P_{HV}). If we assume the leakage of phonons from bottom to top region(top to bottom) as $\eta_{LH}(\eta_{HL})$ with biased voltage of V_{HV} on top region and V_{LV} on bottom region, we can write down the equation for the phonon signals due to an interaction on the LV region of energy E_R, up to first-order correction due to leakage as:

$$P_{HV} = \alpha[(1-\eta_{HL})E_R\frac{V_{HV}L}{\epsilon_{eh}} + \eta_{LH}E_R(1+\frac{V_{LV}L}{\epsilon_{eh}})] \tag{2.1}$$

$$P_{LV} = \beta[(1-\eta_{LH})E_R(1+\frac{V_{LV}L}{\epsilon_{eh}}) + \eta_{HL}E_R\frac{V_{HV}L}{\epsilon_{eh}}] \tag{2.2}$$

Here α and β are the absolute calibration factors for the HV and LV phonon sensors and L is the Lindhard factor which is normalized to 1 for ER events and has an energy dependent fractional

value for NR events. ϵ_{eh} is the average energy to produce an electron-hole pair which is estimated to be 3.8 eV for Si. The first terms for both the equations represent the energy in the Luke phonons generated by the transferred charges and primary phonons in the HV and LV side respectively. The 2nd terms are a first-order correction to the signal due to leakage of phonons from one region to the other.

The discriminator for electron-type and nuclear-type events will be defined as

$$Y = \frac{P_{HV}}{P_{LV}} \tag{2.3}$$

where P_{HV} and P_{LV} are defined earlier. This discriminator is equivalent to the yield in iZIP detectors which discriminates the electron and nuclear recoil events based on the ratio of ionization energy to the total phonon energy.

We can repeat the above line of thought for the events in the high voltage region which will lead to equations similar to the above equations. It is found that the discrimination ratio for the events in the HV region is higher than the ratio for events in the LV region and do not pollute of our region of interest as shown in Figure 2.3

2.2 Detector Simulation

In this section, I will describe the details of determining the exact geometry of the hybrid detector and the different fabrication constraints that goes into optimizing the detector geometry. Further, I will describe the simulation results for the expected electron and nuclear recoil bands using MATLAB.

2.2.1 COMSOL Electric Field Simulation

The idea of the two-stage hybrid detector rely heavily on the efficient transport of the charges from the LV region to the HV region. Since charges will follow electric lines of force in a crystal geometry, we optimized the crystal geometry such that the electric field lines mostly end up on the detector top surface where we have phonon sensors. We used COMSOL Multiphysics software for the detector simulation. Starting from a cylindrical crystal geometry and applying electric field

across the crystal, we found that the ideal detector should be a bell-shaped geometry which would be an engineering challenge at the fabrication level. A second possibility is a conical structure with electric field shapers as shown in Figure 2.2. Note that the housing of the detector is taken into consideration in this simulation which ensures that the simulation is valid in an actual experimental setup. A 3" x 1" dimension Si crystal is considered and the field shapers are made of Cu. There are two electrodes (on top and bottom), not shown in the figure, which are used to apply the biased voltage across the crystal block. There are additional field shaper electrodes around the neck region at 0V which helps to force a few of the electric lines to pass through through the neck region instead of ending on the upper surface of the LV region.

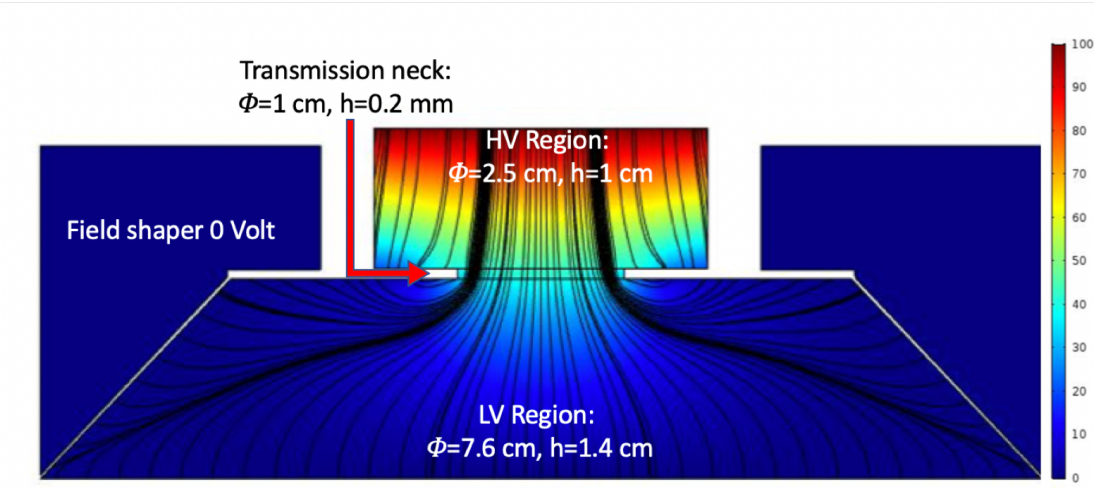

Figure 2.2: Simulation of electrical potential and field lines inside the detector using COMSOL Multiphysics. A bias voltage of 100V is applied from the HV top surface while the potential on the conical field shaper walls and the LV bottom surfaces are held at 0 V

2.2.2 MATLAB Simulation of expected Electron and Nuclear Band

With the optimized geometry as discussed in the earlier section, we can estimate the different parameters of our Hybrid model and simulate the expected electron recoil and nuclear recoil bands. For the conical geometry with 3" of bottom surface(with 2" surface on top side of LV region),

1" top surface and 0.5" neck, the phonon leakage fraction due to geometry(phonon geometric suppression) for phonons leaking from top to bottom side will be $\eta_{HL} = \frac{(0.5)^2}{(1^2)} = 25\%$ and for phonons leaking from bottom to top will be $\eta_{LH} = \frac{(0.5)^2}{(2)^2} = 10\%$. The η_{HL} is taken to be 46% based on results which are obtained in Chapter 4. Other parameters such as $\gamma = \frac{\alpha}{\beta} = 0.788$, $V_{HV} = 9.6$ V and $V_{LV} = 2.4$ V are taken for the simulated bands as shown in Figure 2.3. A uniformly distributed random variable with a gaussian noise is considered as the input for the recoil energy spectrum. The standard deviation of the gaussian noise is kept different for the top and bottom channels which will be helpful later for comparison to the experimental data. The recoiling events at the top region forms a different band of events far from our region of interest, namely the bottom region events.

2.3 Detector Fabrication

CDMS-style detectors are fabricated with techniques borrowed from the semiconductor industry technologies. This usually comprised of selecting a proper substrate, polishing the substrate and etching away different layers of sensor material like Al and W to make micro-structure circuits on the crystal surfaces. The hybrid detector is fabricated using the standard fabrication process in TAMU lab, which is described in detail in Jastram's Thesis [18]. I am going to touch upon the step of making the hybrid geometry which is added on top of the standard process of fabrication for this detector. Since silicon crystals are easier to shape as compared to germanium, the detector material is chosen to be Si for the first prototype.

2.3.1 Detector Geometry Fabrication Process

The fabrication of the hybrid geometry is accomplished with a unique technique devised by our group engineer, Mark Platt. The different steps in this technique can be summarized as

1. The cylindrical crystal is attached to a steel bevel platform as shown in Figure 2.4. This helps in fixing the crystal in a given direction for polishing.

2. The crystal on the bevel platform is aligned at 45° and polished till the shape is fully conical.

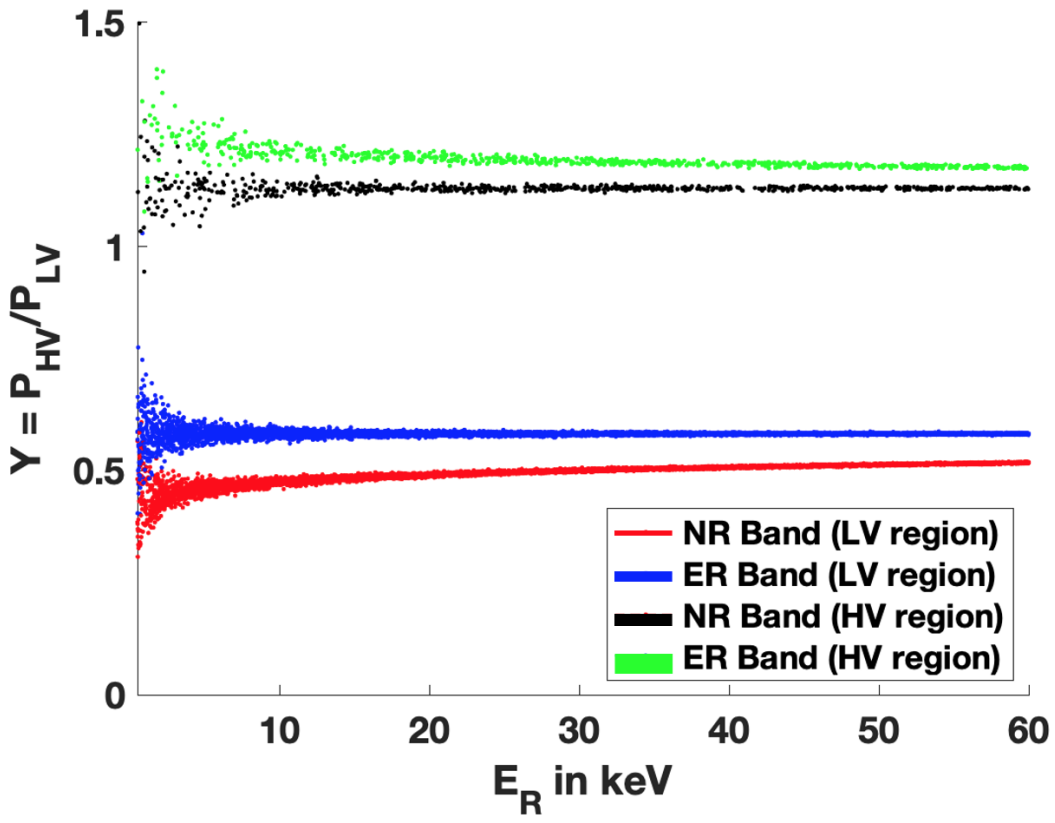

Figure 2.3: Simulation of electron recoil and nuclear recoil events in the hybrid detector. The equation of the hybrid detector is used for the events in the high voltage (HV) and low voltage (LV) region with the two types of recoil, namely electron recoil (ER) and nuclear recoil (NR)

3. The conical crystal is core-drilled from the top surface with a diameter of 1" to make the HV region as shown in Figure 2.4b

4. The crystal is cut through from the sides with a wire-saw to make the neck region.

After the above steps, the crystal goes through the standard process of polishing and etching which yield the final two stage detector as shown in Figure 2.5.

2.3.2 Detector Housing and Phonon Mask Design

SuperCDMS style detector technology demands milli-Kelvin temperatures to work since the phonon sensors have critical temperatures in that range. TAMU lab is well equiped with both cold

(a) Si crystal after grinding in the bevel platform

(b) Si crystal after core-drilling

Figure 2.4: Pictures showing different stages in detector geometry fabrication

Figure 2.5: Fabricated conical detector from cylindrical Si crystal

electronics and fridges to achieve such low temperatures. The detectors are placed inside their own housing frame which are structured into a tower that goes inside the fridge for cooldown. Due to the typical geometry of the hybrid two-stage detector, new housing frames were built ,as shown in Figure 2.6a, which will hold the detector in place as well as provide the necessary infrastructure for detector readout electronics.

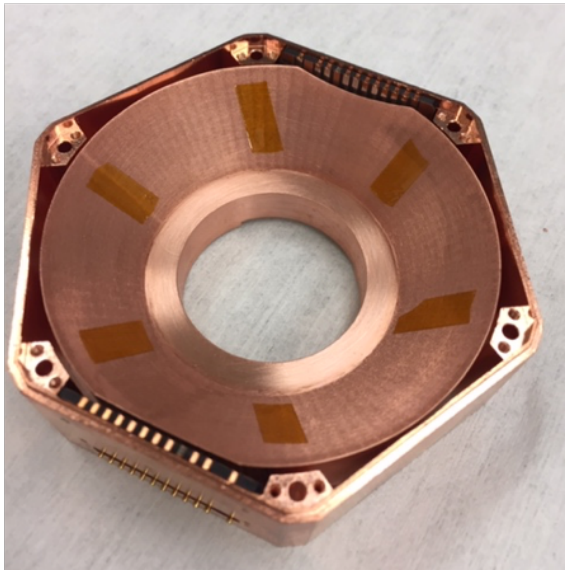

(a) Cone housing to fix the hybrid detector inside detector tower.

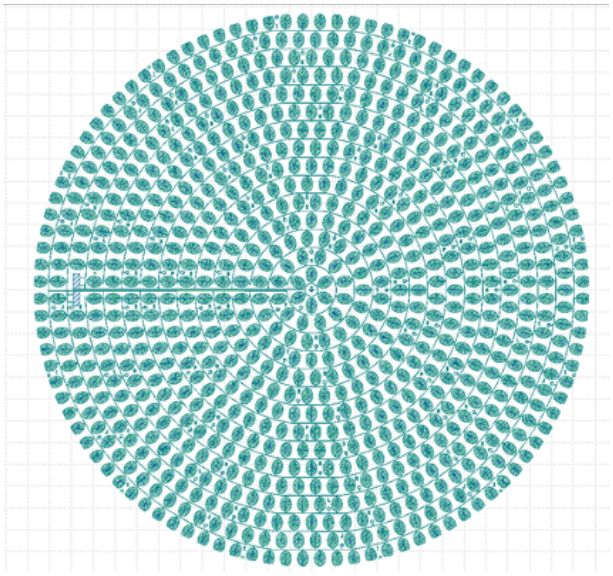

(b) 1” HV mask used for top channel of the hybrid detector

Figure 2.6: Conical detector housing made out of Cu (left) and 1" phonon mask design for the hybrid detector

For phonon readout, a standard 3” SuperCDMS HV mask is used for the bottom side of the hybrid detector. Since the top side of the hybrid is of diameter 1” , there are no standard HV mask. A new HV mask is drawn by editing the center channel of a standard 6 channel HV mask using KLayout software. The 1” cutout channel mask is further edited to have the necessary elements of a typical mask such as alignment marks, etc. Figure 2.6b shows the HV 1” mask which is fabricated on the hybrid detector.

In the previous chapter, I described the theory aspects of the novel hybrid detector. Once the fabrication of the detector is complete, we did multiple experimental runs to establish our predictions and explore vulnerabilities. This chapter is meant to organize the different studies we conducted with the hybrid prototype detector, focusing mainly on the areas of charge and phonon transport, leakage estimates and voltage gradient across the detector, as these are mainly independent studies. I will end the chapter with our current results from the hybrid detector and remarks about our ongoing work.

3.1 Characterizing Charge Transport

Understanding the transport of charges inside the unique geometry of the hybrid detector is critical for accurate prediction of the modulation in the standard physics of a typical CDMS detector. Ramo field simulations were carried out for different orientation and number of electrodes around the crystal which will answer the question of whether we are able to transport the charges all the way to the top region and also to estimate the transport efficiency. Figure 3.1 shows the simulated crystal with one Al electrode on the top side and two electrodes implanted on a PCB board along with their Ramo field and potential.

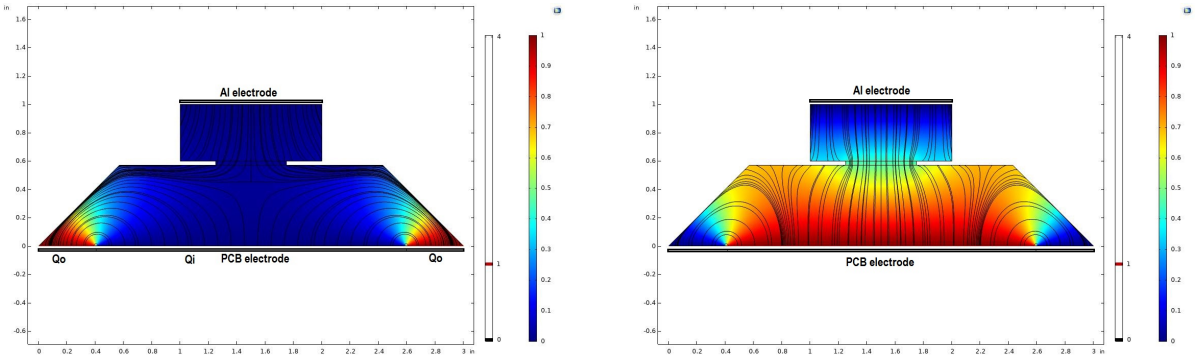

(a) Ramo potential due to Qo (b) Ramo potential due to Qi

Figure 3.1: Ramo potential and associated field inside the Si hybrid detector

To understand the movement of charges in this ramo potential simulation, I will invoke the basic theory of Shockley-Ramo theorem. The charge signal in the electrodes is what the electrodes sense when there is movement of charges as they drift due to the applied electric field in the crystal. The Schockley-Ramo theorem describes the induced current(I) in the electrodes due to this movement of charges, which can be written quantitatively as

$$I = e(\overrightarrow{E}_{electrode} \cdot \overrightarrow{v}) \tag{3.1}$$

where $\overrightarrow{v}$ is the velocity of the charge, e is the amount of charge in Coulombs and $\overrightarrow{E}_{electrode}$ is the electric field in the location of the charge solely due to the electrode. So, in case of an event at a location p_1, if the holes move to location p_2 and electrons move to location p_3 , the total charge signal will be

$$\int I = e[V_{ramo}(p_2) - V_{ramo}(p_1)] \tag{3.2}$$

where $V(x)$ is the ramo potential at the location x.

The charges created near the edge(sidewalls) of the bottom region of the hybrid will be sensed primarily by the outer electrode(Q_o) and the bulk events will have a pronounced signal on the Q_i electrode. Since the ramo field between the electrodes as in Figure 3.1a is well defined, it is expected that there will be sharing of energy for interactions in the bulk. The amplitude of energy sharing for different regions of the detector tells about the efficiency of charge transport since a low charge transport will lead to a drop in amplitude of the signal when we look at events from different parts of the detector.

3.1.1 Setup for measuring charge signal

For the charge transport study, the bare fabricated Si crystal with no phonon sensors is kept in a contact-free setup inside a wet fridge hosted by Glenn Agnolet/Nader Mirabolfathi. An Aluminum electrode is kept on the top surface to provide the applied bias voltage across the detector and a PCB board with two electrodes Q_{inner}(Qi) and Q_{outer}(Qo) are kept on the bottom side of the hybrid, which are connected further to the CDMS electronics to readout the charge .An ^{241}Am

source was attached to the PCB electrode collimated to an event rate of 1 Hz. A hole of diameter 0.07 mm is made in the PCB board aligning the source to allow lower energy X-rays from the source to reach the detector surface. During operation, the fridge reached a temperature of approx. 12 mK. The data is taken with a CAEN digitizer controlled by a Labview VI.

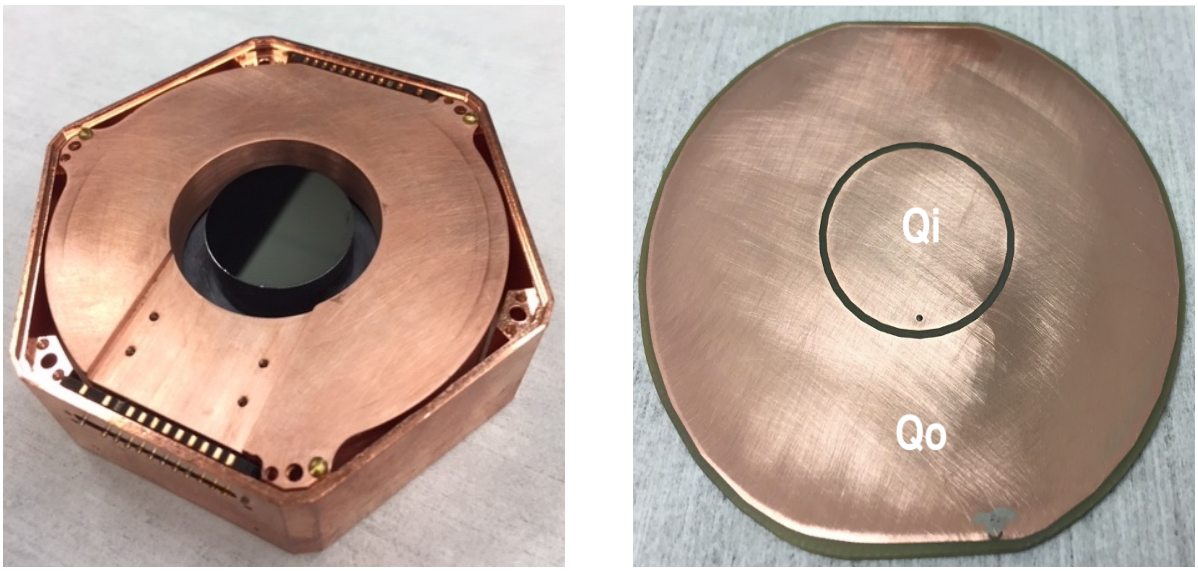

(a) Hybrid detector inside the Cu housing for contact-free study

(b) PCB board with the inner (Qi) and outer electrode(Qo)

Figure 3.2: The Hybrid detector inside the Cu-housing for contact-free setup (left) and the readout electrode (right) to measure charge signal

3.1.2 Data taking procedure for Charge Transport study

The charge traces saved by the Labview VI is processed with indigeneously written python scripts, utilizing QETpy package developed by the Berkeley Group for Optimal Filtering. The package takes in the raw traces along with a template for noise/pulse and outputs the amplitude of the trace along with its χ^2 of fitting the template to that trace. The final output of the python scripts are ROOT files which are further analyzed with plotting scripts.

Since every charge pulse is identical to each other in shape, pulse templates are created by averaging a selected group of pulses for a given voltage based on criteria such as low pre-pulse

standard deviation, small post-pulse standard deviation etc. Further details about the data analysis scheme is discussed in Section 3.2.2

Multiple sets of data in increasing bias voltage were taken starting from 100V to 400V. Both positive and negative bias voltage were applied to check for ambiguity. After every set of data, the detector is grounded and led flashing was done to ensure proper neutralization of the detector.

3.1.3 Results from Charge Transport Study

Figure 3.3a show the reconstructed spectrum of ^{241}Am source from the hybrid detector by summing over the Qi and Qo amplitudes of the traces. The distinct peak of 60 keV line is fitted with a gaussian function on an exponential background. A small non-resolvable population of low energy X-rays is also observed in the spectrum.

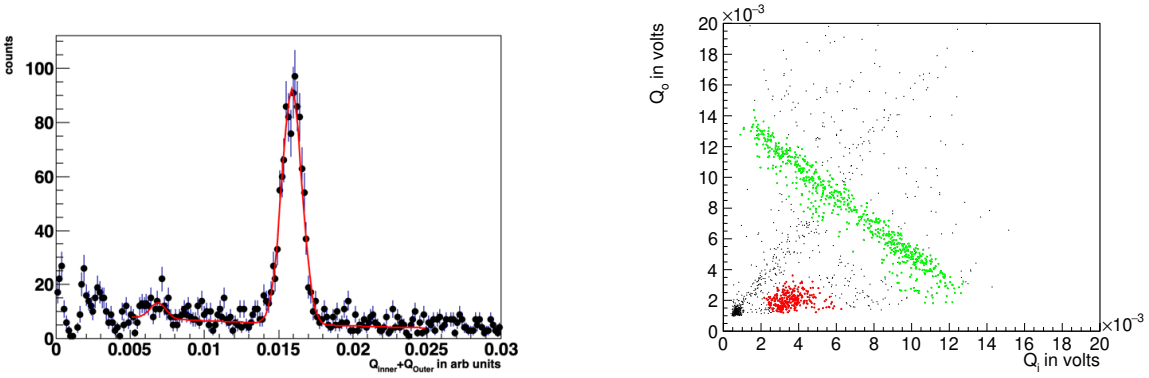

(a) ^{241}Am spectrum obtained by summing over the charge channels Qi and Qo

(b) 2D plot of charge amplitude on Qi vs charge amplitude on Qo

Figure 3.3: Charge Transport Study in contact-free Si hybrid detector for biased voltage of 100V. The 60 keV events are shaded in green and the small population of lower energy X-rays are shaded in red.

Figure 3.3b also shows the 2D plot of the amplitude of charge collected in the inner electrode vs the outer electrode. The 60 keV events(shaded in green) are shared between the two electrodes due to their large mean free path($\mu_{Si,58.49keV} = 0.77cm^{-1}$) while the lower energy X-rays(11 to 26 keV) are concentrated in Qi due to relatively smaller mean free path. The raw amplitude of the

60 keV events are similar on both the electrodes which points to fact that we are close to 100% charge collection efficiency at 100V. It also establishes the fact that we can transport charges from the bottom region to the top region through the neck.

We also noted that a small population of events are along the diagonal in the 2D plot which indicates that these events have positive correlation for both the electrodes. These events are estimated to be events happening in the top region of the detector.

3.2 Phonon Transport Study

Having established that charges can transport in the two stage hybrid detector, I will discuss the results from runs dedicated to understand the transport of phonons in this detector. To prepare the hybrid detector for phonon readout, a 3" HV mask with four phonon channels, is fabricated on the bottom side of the detector. A newly developed 1" mask is fabricated on the top side of the detector having one channel. Since the standard electronics connection in the housing is traditionally made for 3" only detectors, a PCB board is fixed on the side of the housing as shown in Figure 3.4a to bridge the gap. Figure 3.4 also shows the hybrid detector with the fabricated masks on both the sides.

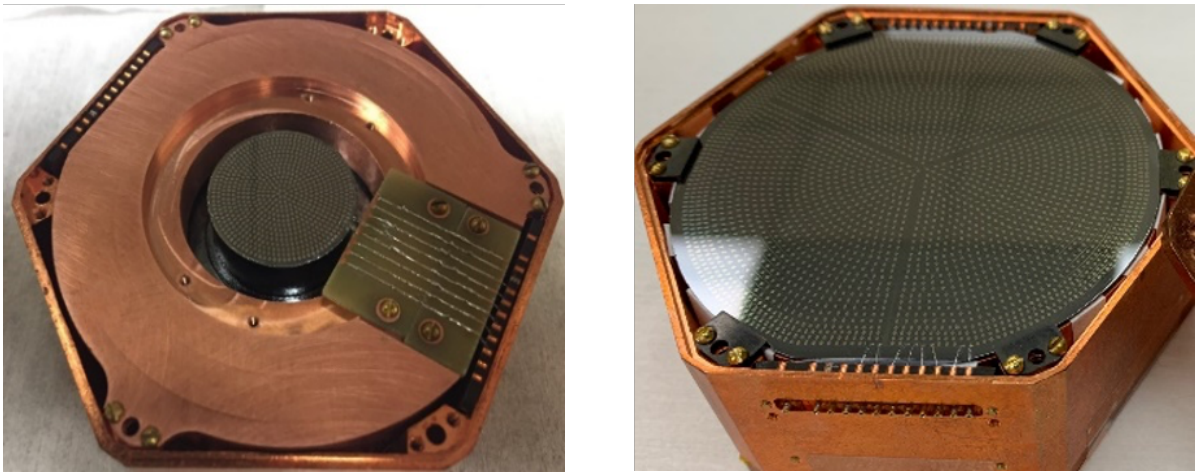

(a) Hybrid detector with 1" phonon HV mask

(b) Hybrid detector with 3" phonon HV mask

Figure 3.4: Fabricated Hybrid detector prototype with phonon masks on top and bottom side.

Two internal sources are used to calibrate the top and bottom side of the detector. An ^{55}Fe source is kept at the center region of the top phonon mask, attached to a housing lid where the detector was held. An ^{241}Am source is kept facing the bottom 3" mask of the detector, inside a collimator attached to the bottom housing lid. The sources were tuned to 6 Hz for ^{55}Fe and 5 Hz for ^{241}Am using a room temperature silicon drift detector(SDD). The hybrid detector inside the housing is kept in a tower assembly which is held in a 10 mK stage of a BlueFors fridge available at the TAMU testing facility.

3.2.1 Setup for biasing phonon only detectors

In a traditional setup, phonon readout in CDMS detectors are done using a circuit as shown in the Figure 1.6. This cold electronics further connects to warm electronics in the circuit containing Front-End Board(FEB) which host the amplifiers, SQUID biasing etc. and Receiver-Trigger-Filter(RTF) board which filters the signal and provide trigger conditions for the digitizers. The inherent issue with the circuit is that the phonon sensors are held at ground potential. To provide a bias voltage across the hybrid detector along with maintaining QET bias current, the standard warm electronics need to be bypassed for the top channel. So, the phonon sensors on the top channel are directly biased externally with a circuit as shown in Figure 3.5 which helps in voltage biasing the detector as well as to maintain a fix QET bias current for the phonon sensors.

The inner three channels (labelled as B,C and D) are considered in this run. The outermost channel(labelled as Channel A of the HV mask) is kept at floating potential. The main reason for not using the outermost channel was dependent on the number of SQUETs available to connect the phonon channels. The outermost channel was readout in later runs which will be discussed in Chapter 4. The bottom channels of the hybrid detector are connected to the standard CDMS cold and warm electronics circuit. For data acquisition, a 14-bit CAEN digitizer with 8 channel input(Model: V1724) is used which reads in data through a Labview interface and save it as text files.

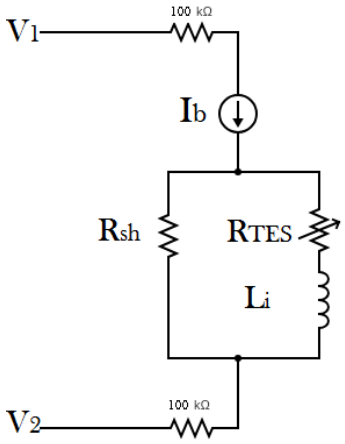

Figure 3.5: External biasing scheme for hybrid top channel. V_1 and V_2 are external voltage source connected through two 100 kΩ resistors to the QET bias circuit

3.2.2 Optimal Filter and Data Analysis Scheme

Optimal Filter algorithm is used to extract the pulse amplitude and time information from the data. This method works based on the fact that signal information is contained in certain portion of the bandwidth of the frequency spectrum while noise dominates a separate portion, and we can maximize the signal-to-noise rejection by weighting in the expected signal-to-noise in the frequency domain. Since the noise in our readout circuits are correlated in time, a simple χ^2 minimization in time domain won't give an accurate solution which is the basis to chose this OF method over the latter.

For the analysis of both charge as well as phonon signals, the Optimal filtering package is provided with the following:

1. the raw traces from the digitizer of given sampling frequency

2. a pulse template made by averaging multiple pulse traces from the same dataset, chosen based on pulse selection criteria such as small pre-pulse and post-pulse standard deviation, a reasonable low value of minima of the pulse and tail of the pulse(last few hundred bins) to be small.

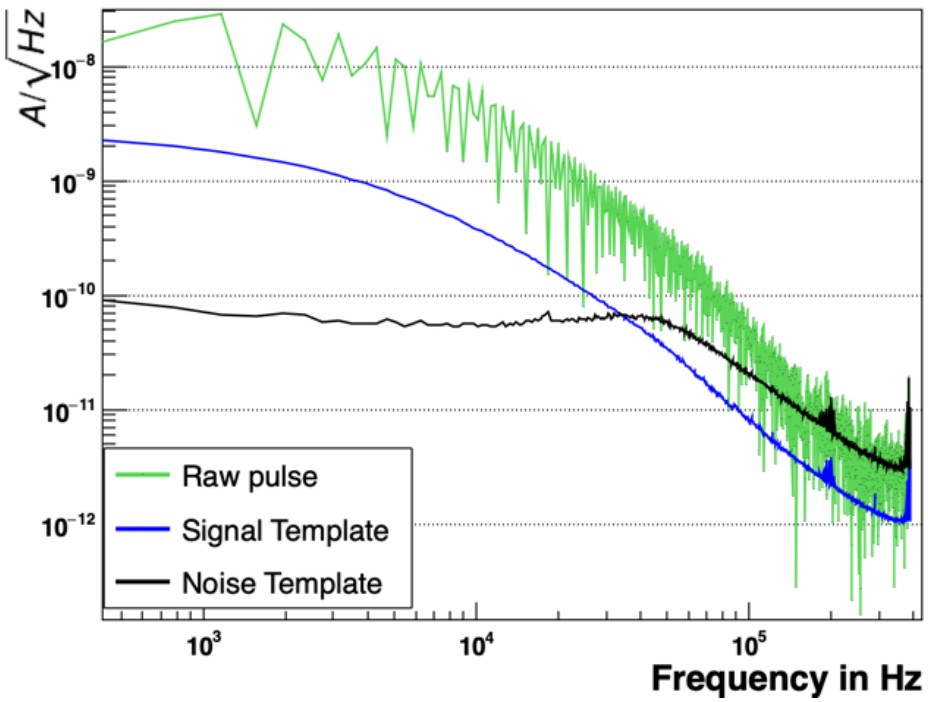

Figure 3.6: Signal, noise and raw pulse spectra for a typical phonon pulse in the hybrid detector (example pulse for top phonon channel)

3. a noise template which is made by choosing randomly triggered traces in the dataset and further filtering them based on low overall standard deviation and maximum value of the trace. This is done to remove traces with pulses in them while making the noise template.

As shown in Figure 3.6 and 3.7 , the time series of raw pulses S(t) and signal template A(t) is converted to frequency domain($\widetilde{S}$ notation represents the Fourier transform of S) by a FFT(Discrete Fourier Transform is used since traces are sampled in time-bins). Given a noise frequency distribution $J(f)$ with frequency f, satisfying $J(f) =< \widetilde{N}^2(f) >$ where N(t) is the noise amplitude in time-domain, the χ^2 will be given by

$$\chi^2(A) = \sum_n \frac{|\widetilde{S}_n - Ae^{2\pi i t_0 f_n}\widetilde{A}_n|^2}{J_n} \tag{3.3}$$

and the minimization procedure will lead to a best-fit value of A as

$$A = \frac{\sum_n \frac{\tilde{A}_n \tilde{S}_n}{J_n}}{\sum_n \frac{|\tilde{A}_n|^2}{J_n}} \tag{3.4}$$

Though the above equation finds the optimal value of the amplitude A, the task is to minimize $\chi^2(A, t_0)$ in 2D space of A and t_0. In CDMS, A is computed for many values of t_0 and the maximum $A(t_0)$ is chosen. Note that in case of multiple maxima, this value will correspond to any of the multiple minima of χ^2, not necessarily the smallest minima.

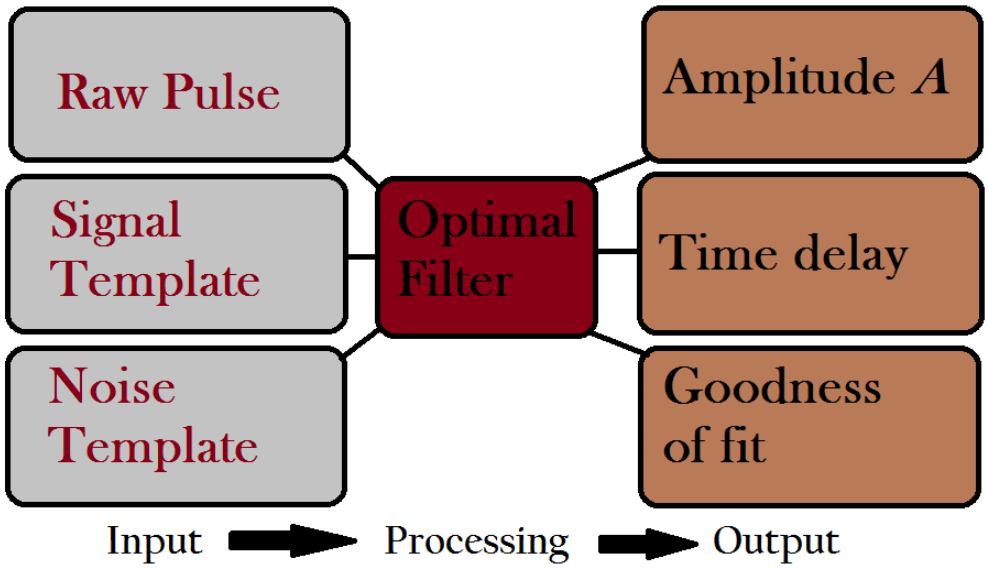

Figure 3.7: Schematic diagram of the input parameters and the output results in the Optimal Filter algorithm

The output from the package is the pulse amplitude (A), pulse start-time(t_0) and χ^2 of fitting the pulse trace to the pulse template. Note that unlike charge traces, phonon pulse shape has a wealth of information and varies based on detector physics. So, the averaging of the pulse traces is done to ensure that the pulse template can be used for all pulse shapes in the dataset.

The pulse amplitudes of the bottom phonon channels of the hybrid detector are summed up to

give a total phonon amplitude(P_{LV}) and the top channel phonon amplitude is termed as P_{HV}. In the analysis presented in this chapter, the integral of the pulse is used instead of the optimal filtered output which compensates for saturated pulses at higher energies. These quantities are in current units(Ampere) which need to scaled by calibration factors to convert into energy units. The 60 keV line in the spectrum from ^{241}Am source on the bottom side of the detector and the 5.9 keV line from the 55Fe source on the top side of the detector is used for energy calibrations.

The three inner phonon amplitudes of the bottom channels of the hybrid detector can be combined into a position based energy partition variable using the following relations:

$$Xpart = \frac{\cos(30)pd + \cos(150)pb + \cos(270)pc}{pd + pb + pc} \tag{3.5}$$

$$Ypart = \frac{\sin(30)pd + \sin(150)pb + \sin(270)pc}{pd + pb + pc} \tag{3.6}$$

where pb, pc and pd are the phonon amplitudes of the inner channels of the bottom face of the hybrid detector(labelled as B, C and D). From these two quantities, a radial partition quantity can be defined as $Rpart = \sqrt{(Xpart)^2 + (Ypart)^2}$

Since phonons propagate through the detector diffusively, they tend to have some time delay with respect to the trigger time of the event. This time delay between arrival of phonons can be measured on a channel-to-channel basis. In CDMS detectors, the charge signal is used as a reference for calculating the delay time of the phonon pulses. In the hybrid, the trigger time of the digitizer which is set at 40% of the pulse trace is taken as the reference point. A similar x-y partition variable for relative delay between the phonon signals in the inner channels of the bottom face of the hybrid can be constructed. The delay time for each phonon channel is calculated based on the time difference between the 40% point of the pulse trace to the 20% risetime of the pulse and the delay time for the channels are combined into delayX and delayY as defined below:

$$delayX = \frac{\cos(30)dD + \cos(150)dB + \cos(270)dC}{dD + dB + dC} \tag{3.7}$$

$$delayY = \frac{\sin(30)dD + \sin(150)dB + \sin(270)dC}{dD + dB + dC} \tag{3.8}$$

where dB,dC and dD are the delay time for the inner channels on the bottom face of the hybrid detector(labelled as B,C and D). A radial delay variable can be defined following the same recipe as in the previous case as $Rdelay = \sqrt{(delayX)^2 + (delayY)^2}$.

3.2.3 Noise Performance

Noise datasets are taken at the beginning of each data taking run with random triggering mode of the DAQ VI. The overall noise level is found to be $\sim 10^{-10}$ A/$\sqrt{Hz}$ in the experimental setup used here, as shown in Figure 3.8. This noise template is further feed into the Optimal Filter algorithm for pulse data analysis.

3.2.4 Unbiased detector Results

With the data analysis strategy defined in the previous section, we looked at the unbiased voltage measurements with only internal sources. In Figure 3.9, a two-dimensional plot of the raw amplitudes of P_{HV} versus P_{LV} is shown. There are two distinct band of events, each corresponding to the two regions of the detector. The 60 keV line from ^{241}Am source can be seen in both these regions, forming two distinct blob of events. The 5.9 keV from the ^{55}Fe source forms another unique blob on the top region band. The leakage of phonons from one region to the other can be inferred from the way these bands are slightly tilted towards the diagonal. Also shown in Figure 3.10 are the distribution of the bottom region events in the energy partition and phonon delay variables derived earlier. The events in the bottom region of the detector are forming a triangular shape in the energy partition mainly due to physical arrangement of the three inner phonon channels as forming parts of a circle.

3.2.4.1 Calculation of η_{HL} and η_{LH}

Let us denote the 60 keV events in the top and the bottom region by (PH_1, PL_1) and (PH_2, PL_2) respectively, where $PH_{1,2}$ denotes the amplitude of the phonon signal on the HV channel

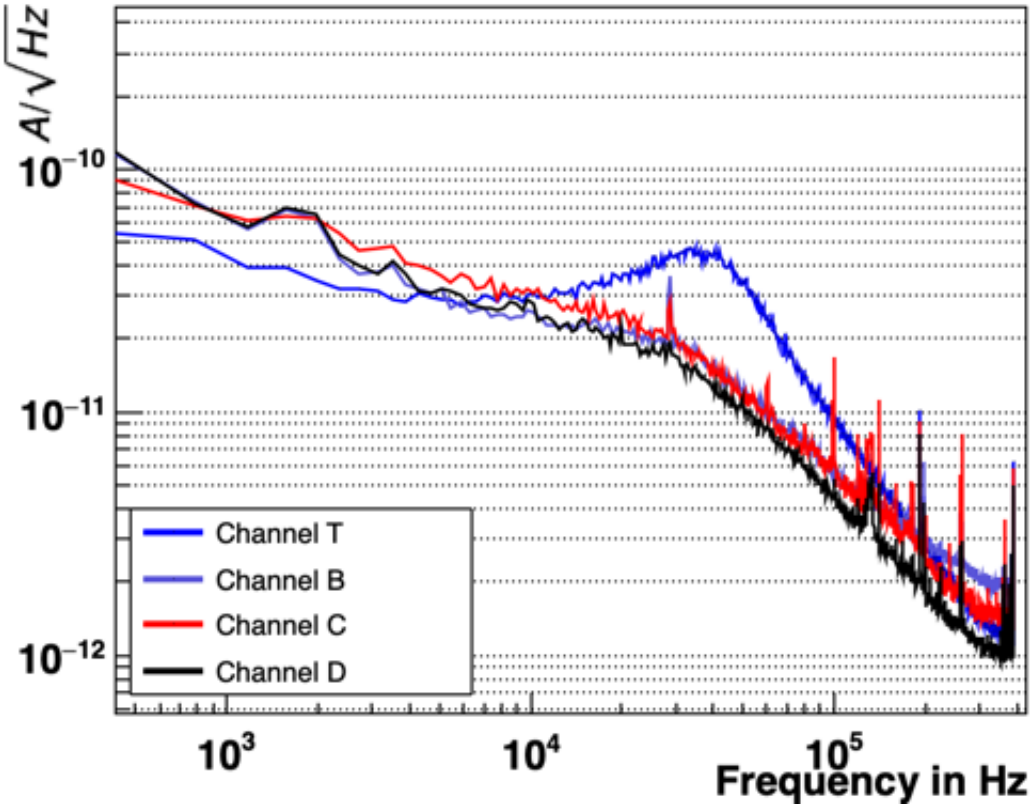

Figure 3.8: NoisePSD for top channel T and three inner channels (B, C, D) on the bottom side of the hybrid detector at a detector bias voltage of 0V

and $PL_{1,2}$ denotes the total amplitude of the phonon signal on the LV channel. Since 60 keV events are selected for this method, E_R is a constant in this case. The equations for the hybrid detector at 0V for top region events will be

$$\begin{aligned} P_{HV} &= \alpha(1-\eta_{HL})E_R \\ P_{LV} &= \beta\eta_{HL}E_R \end{aligned} \tag{3.9}$$

and the corresponding equations for the events in the bottom region will be

$$\begin{aligned} P_{HV} &= \alpha\eta_{LH}E_R \\ P_{LV} &= \beta(1-\eta_{LH})E_R \end{aligned} \tag{3.10}$$

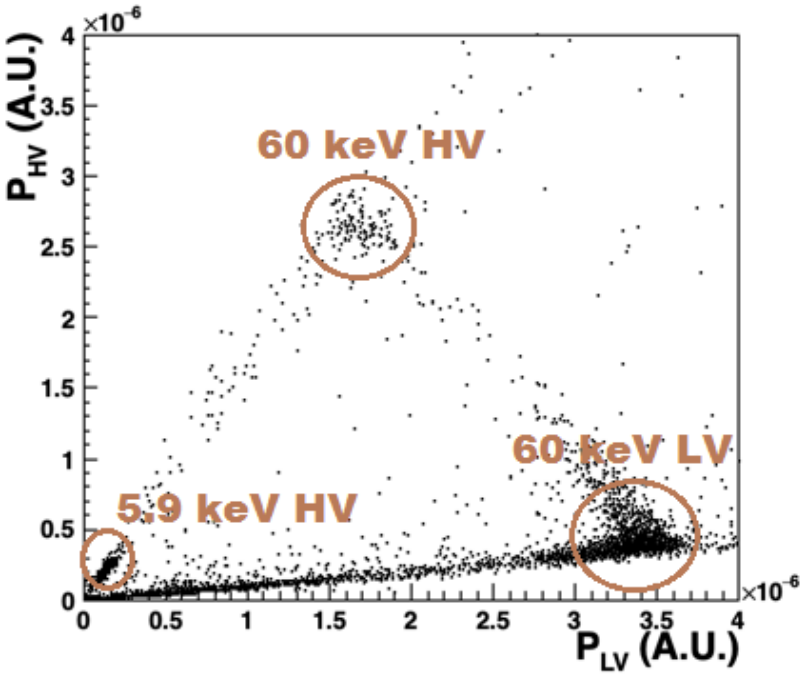

Figure 3.9: Two-dimensional plot of amplitude of the top and bottom phonon channels of the hybrid detector at 0V. The 5.9 keV and 60 keV events on the top and bottom region are circled in red.

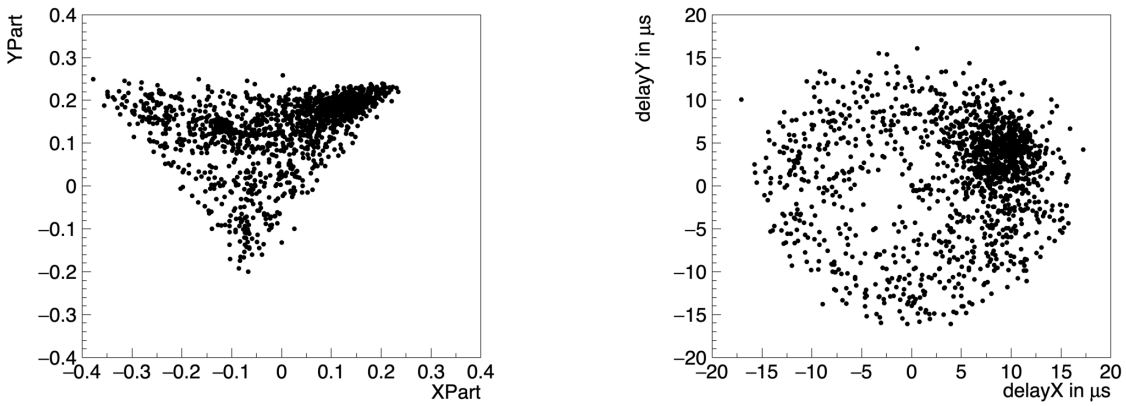

(a) Partition plot showing the energy distribution of events in the bottom region.

(b) Delay plot showing the timing distribution of events in the bottom region.

Figure 3.10: Distribution of the 0V events in the bottom channel in terms of energy partition (left) and phonon delay (right) variables. The accumulation of events in the top right corner is due to presence of an ^{241}Am source on Channel D

Dividing the above equations to eliminate α and β and writing two new parameters l and h defined as

$$\begin{aligned} l &= \frac{1-\eta_{HL}}{\eta_{LH}} \\ h &= \frac{\eta_{HL}}{1-\eta_{LH}} \end{aligned} \tag{3.11}$$

we can solve the linear equations to find the values of η_{HL} and η_{LH} as following:

$$\begin{aligned} \eta_{HL} &= \frac{h(l-1)}{l-h} \\ \eta_{LH} &= \frac{1-h}{l-h} \end{aligned} \tag{3.12}$$

With a known value of phonon leakage fraction from above, the phonon calibration factors α and β can be calculated using

$$\frac{\alpha}{\beta} = \frac{PH_1}{PL_1}\frac{1-\eta_{LH}}{\eta_{LH}} \tag{3.13}$$

Plugging down the amplitude of the 60 keV events on the top and bottom region at 0V in Figure 3.9, we can find the following parameters for the model:

1. leakage fraction from top to bottom region, η_{HL} = $(46 \pm 2)\%$
2. leakage fraction from bottom to top region, η_{LH} = $(10 \pm 2)\%$
3. absolute phonon calibration factor, $\gamma = \frac{\alpha}{\beta}$ = $1.33 \pm .5$

3.2.4.2 Calculation of Phonon baseline resolution

The phonon baseline resolution can be readily calculate based on the above parameters. Using the OF filter algorithm, dedicated noise traces are feed into the raw traces input for the package and the histogram of the amplitude distribution for the the top and bottom channels are obtained. The distributions are calibrated in terms of energy by using the 60 keV(and 5.9 keV for top) amplitude $E_{H/L}$ of the bottom channel from Figure 3.9 and using the conversion relation $E_{keV} = E_{amp} \times \frac{E_R(1-\eta_{HL/LH})}{E_{H/L}}$. The standard deviation of the fitted gaussian on the distribution yields the

phonon baseline resolutions, which are shown in Figure 3.11.

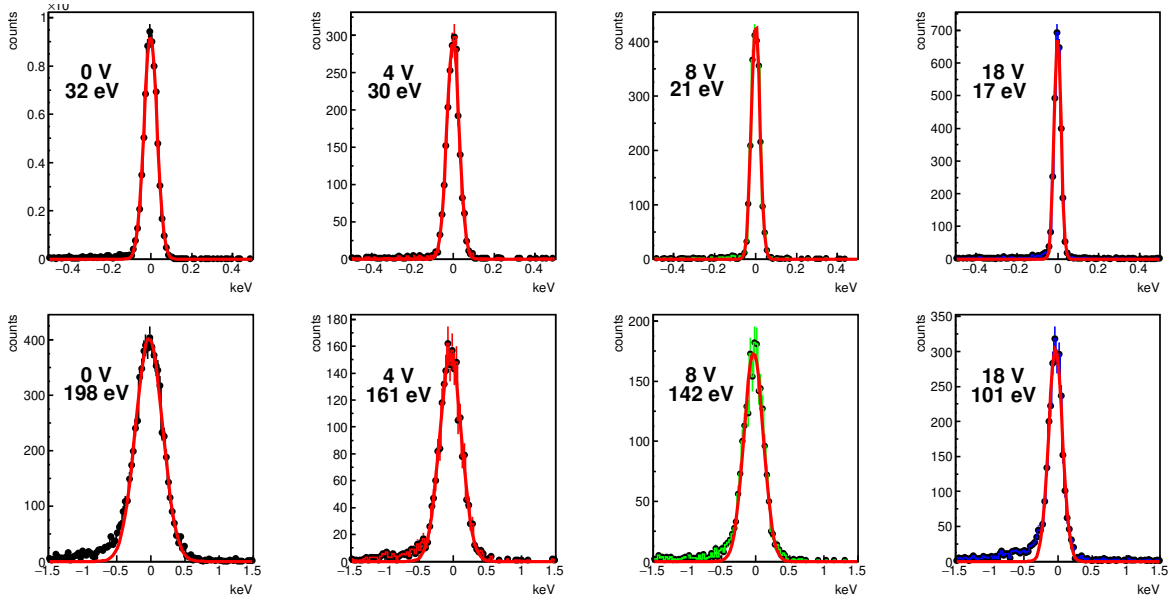

Figure 3.11: Phonon baseline resolutions of the top (top row) and bottom (bottom row) channels for the hybrid detector at different biased voltages.

The baseline resolution (BR) as a function of voltage can be parameterized as

$$BR = \frac{N_0 + (bV)}{S_0 + n_{eh} S_0} \tag{3.14}$$

where S_0 is the signal amplitude in Ampere, N_0 is the baseline resolution in Ampere, b is the shot noise in the system, n_{eh} is the number of electron hole pairs and V is the applied voltage bias. Since we are dealing with electron recoils in this case, n_{eh} is simply $\frac{eV}{\epsilon}$ where $\epsilon = 3.8$ eV for Si. Figure 3.12 shows the fitted function for the top and bottom channel for the hybrid detector. The voltage parameters can be found using the estimated parameter values and applying it on a voltage-bias dataset. In Figure 3.13, the distribution of ^{57}Co events for the parameter V_{HV} in a 12V biased voltage set is shown. The peak value of $9.72 \pm .02$V is taken as the effective voltage drop over the top region of the detector.

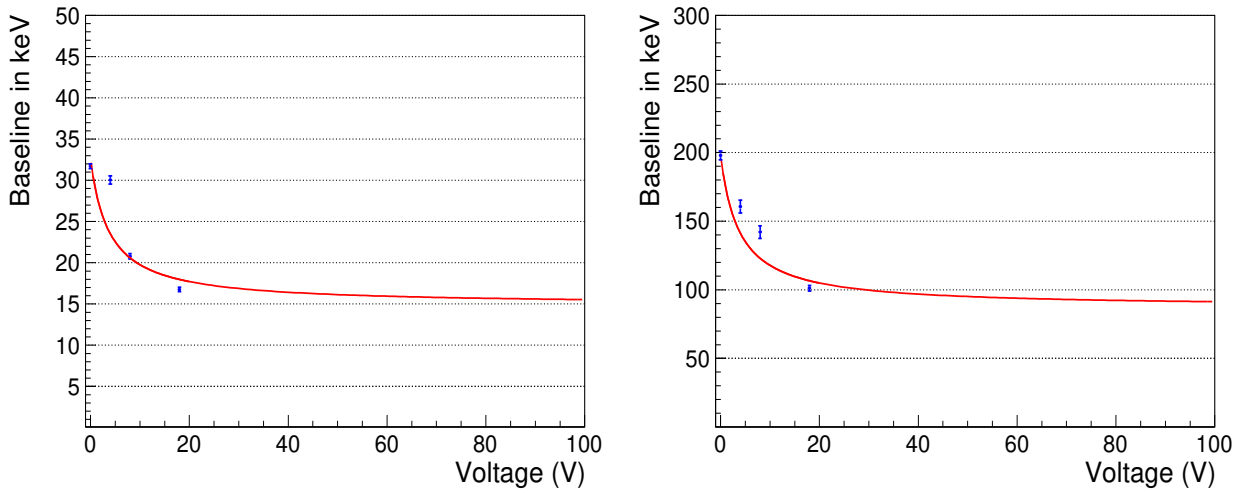

(a) (b)

Figure 3.12: Phonon baseline resolution as a function of biased voltage for the (a) top side and (b) bottom side of the hybrid detector. The fitted functional form given in Equation 3.14 is shown in red color.

3.2.5 High Voltage Results

Using the external QET biasing scheme discussed in Section 3.2.1, the hybrid detector is biased for different voltages with only internal sources and the NTL linearity of the identifiable peaks are verified. The events corresponding to the 6 keV line of ^{55}Fe for the top side and 59.5 keV line of ^{241}Am for the bottom side of the detector is selected and plotted as a function of different detector voltages as shown in Figure 3.14. It is seen that the bottom channel is linear in this region of voltage, but the top channel losses linearity pretty quickly. This can be attributed to the small number of phonon sensors on the top surface which leads to a quick saturation of the QET sensors. This implies that the dynamic range for the detector is low as compared to HV detectors but the primary purpose of the hybrid detector is to look for low energy recoils which will not need very high dynamic ranges.

In Run No. 11 at Mitchell Physics Lab Facility, multiple datasets are taken with the hybrid detector in presence of a ^{57}Co radioactive source which gives only electron recoil events and a ^{252}Cf source which decays to give both gammas (electron recoils) and neutrons (nuclear recoils). The

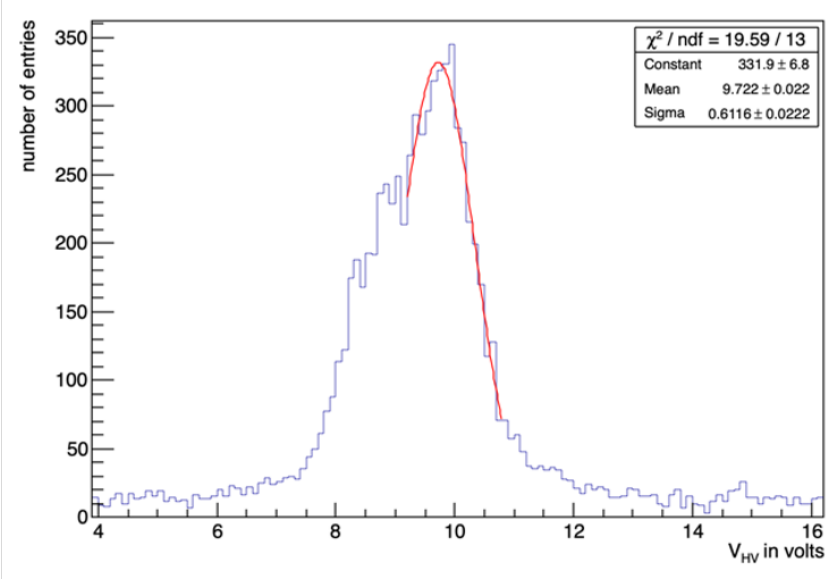

Figure 3.13: Histogram of events for the calculation of effective voltage drop across the top region of the hybrid detector

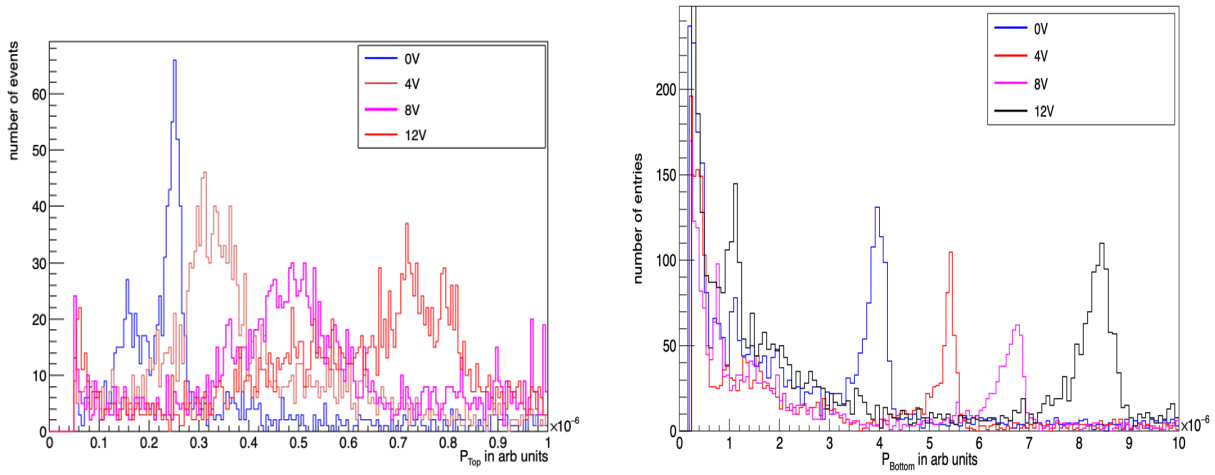

(a) 6 keV peak from ^{55}Fe source at different voltages (b) 59.5 keV line from ^{241}Am source at different voltages

Figure 3.14: Plot showing the linearity of the Luke phonons as a function of detector voltage on the (a) top and (b) bottom side of the hybrid detector

source is kept about 4" away from the fridge housing the detector at the same level as the detector stack. The top side of the hybrid detector was externally biased with a voltage configuration of

$V_1 = +19$V and $V_2 = +5$V, which provides a QET bias current of 70 μA with a detector bias voltage of 12 V. Data analysis is performed using the procedure described in Section 3.2.2 and the raw amplitude of the ratio of the signal from the top and bottom side of the detector is plotted as a function of total amplitude(equivalent to total energy of the event) of the signal on the bottom side as shown in Figure 3.15 where the x-axis is calibrated to the 60 keV line of the source. In general, the amount of ionization energy from a nuclear-type and electron recoil type event is different for a given deposited energy event which helps in discriminating the two type of interactions. It is found that the ionization energy is lower (Lindhard suppressed) for nuclear recoil events. Please note that the events are not corrected for Lindhard suppression in Figure 3.15 . We see one band of events in case of the ^{57}Co source which will be denoted as the electron recoil(ER) band and two band of events in presence of the ^{252}Cf source. Since the top band of events are aligned with the ER band of the ^{57}Co source, we can quickly assign these events to be the ER band for ^{252}Cf source gammas and the lower band to be Lindhard-suppressed nuclear recoil events from ^{252}Cf neutrons.

For higher statistics, multiple sets of ^{252}Cf datasets are merged. The electron recoil band and nuclear recoil band is defined by making bins in energy(x-axis in Figure 3.15) and projecting the events of each bin to yield axis(y-axis), and fitting the 1D histogram with a gaussian function. The fitted mean and sigma of the gaussians for the energy bins are further fitted with a function of the form $f(E) = a + b/E^2$, assuming a quadratic dependence of the standard deviation with energy(E). All events below 1σ of the electron recoil band is selected for Lindhard correction. Using the standard value of Lindhard, $L_{Si} = 0.146$ (for simplicity) the correction to energy is done using

$$E_R = \frac{P_{LV}}{\beta[(1-\eta_{LH})E_R(1+\frac{V_{LV}L_{Si}}{\epsilon_{eh}}) + \eta_{HL}E_R\frac{V_{HV}L_{Si}}{\epsilon_{eh}}} \tag{3.15}$$

where the values for the parameters of the model are calculated in previous sections. The events in the nuclear recoil region will shift in energy due to this correction and a nuclear recoil band is recalculated using a similar approach as described in the last paragraph. With Lindhard corrected nuclear recoil events, the x-axis of the graph can be relabelled as true recoil energy(E_R) as shown in Figure 3.16. Also shown are the 1σ bands for the electron recoil and nuclear recoil events.

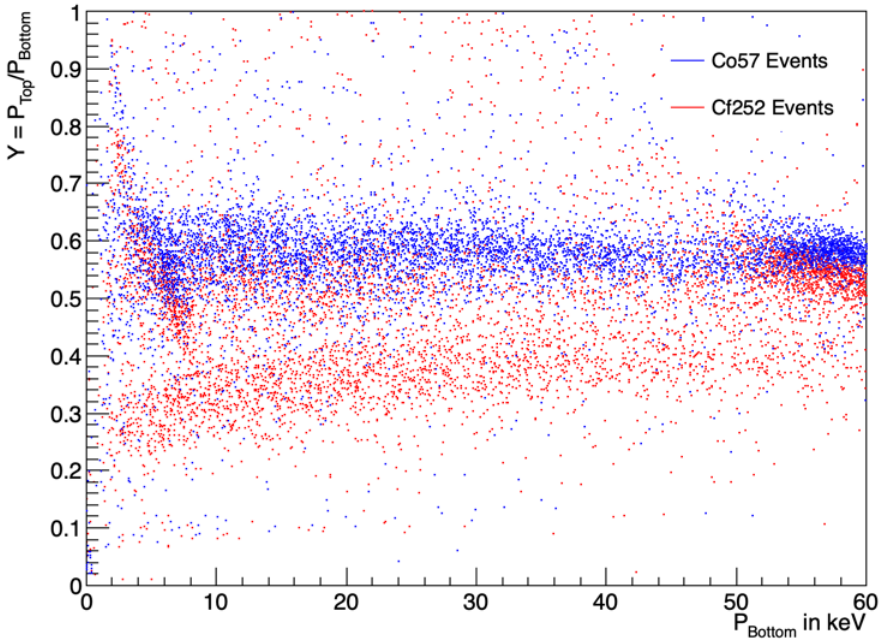

Figure 3.15: Yield plot (without Lindhard correction) of electron recoil events from ^{57}Co radioactive source(in blue) superimposed with electron and nuclear recoil events from ^{252}Cf source(in red). Note that the discrimination between the two type of events improve at lower energies.

The distribution of these selected electron recoil and nuclear recoil events in the delay plot is shown in Figure 3.17. This shows that there is an inherent difference in timing information between electron recoil and nuclear recoil events, which is consistent with earlier CDMS results. The two delay variables can be combined into $rdelay$ variable without loss of information as shown in Figure 3.17b.

Following a similar procedure as described in Jeff Fillippini's thesis [19], the three parameters: $rdelay$, P_{HV} and P_{LV} are combined into a χ^2 analysis test which is a statistical technique to separate out the background(electron recoil in our case) from the signal events. Figure 3.18 shows the distribution of electron recoil and nuclear recoil events in the parameter space of signal χ^2_N and background χ^2_B with detailed analysis steps given in Appendix A.

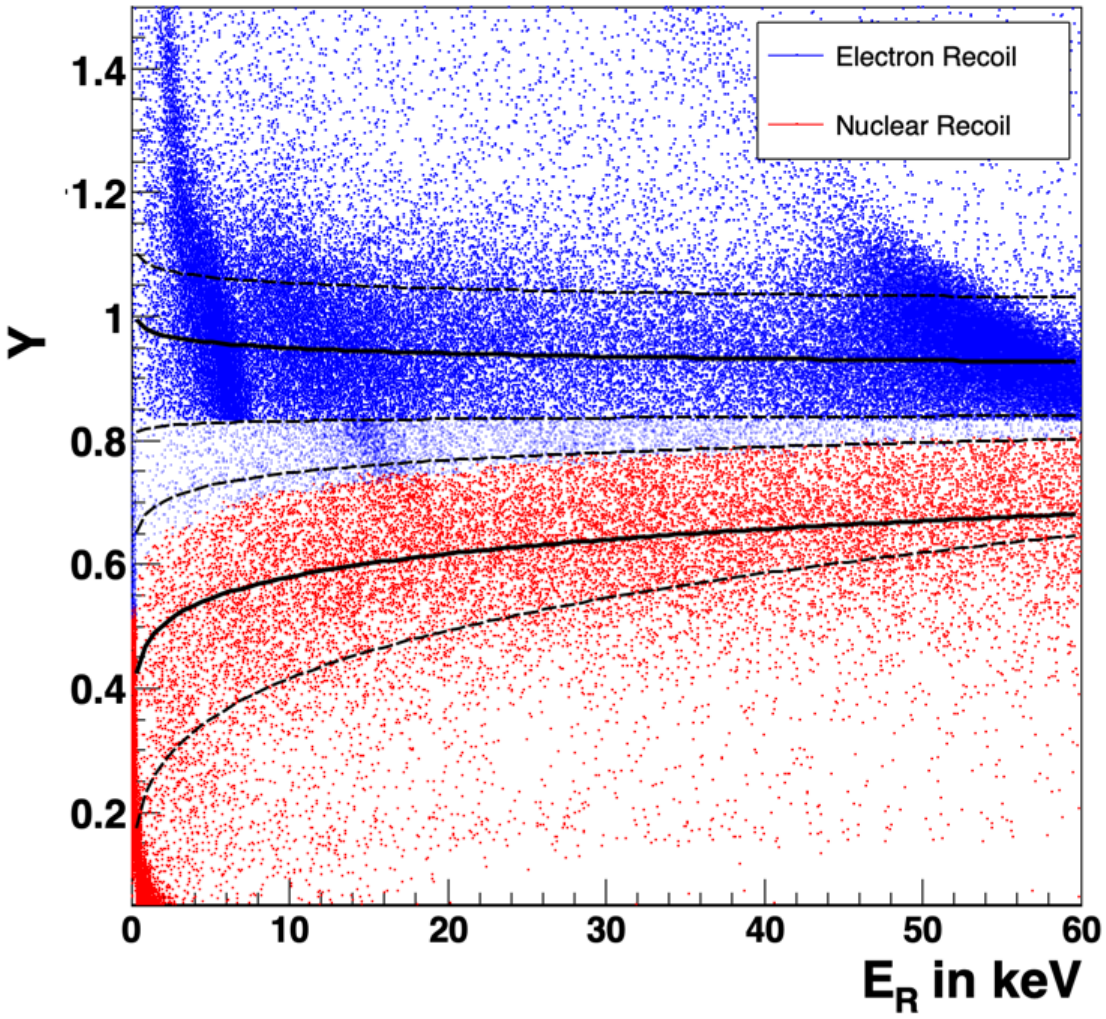

Figure 3.16: Yield plot (with Lindhard correction) of recoil events from ^{252}Cf source. Black Solid line is the fitted gaussian mean of the electron recoil(in blue) and nuclear recoil(in red) bands respectively. Black dotted lines are the 1σ away from the gaussian mean for the two bands. The events in between the bands are colored in light blue.

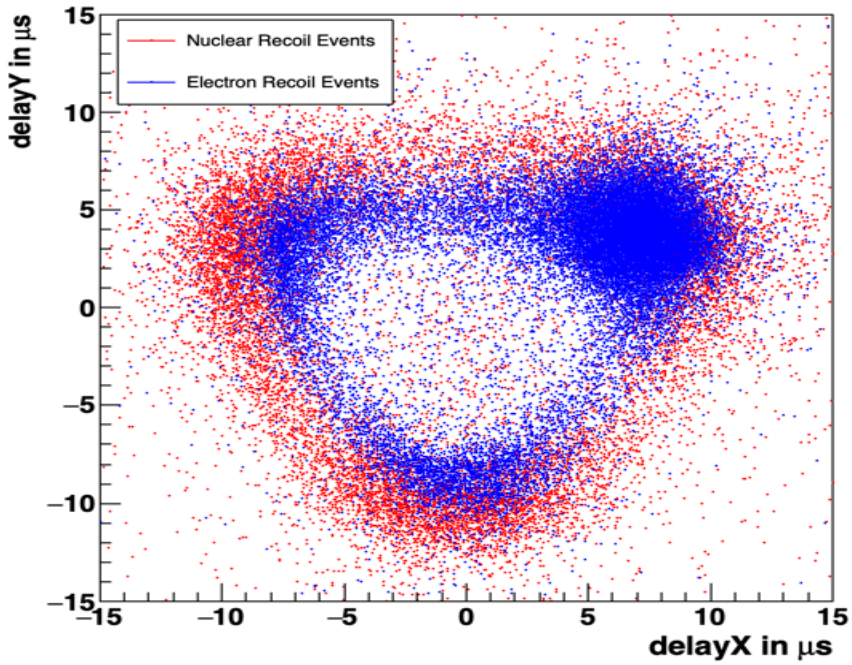

(a)

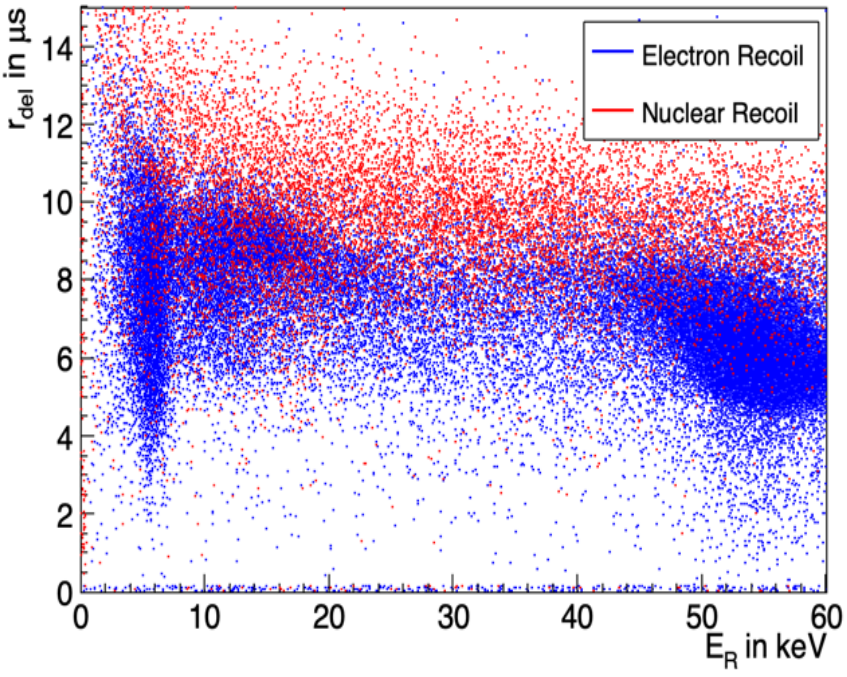

(b)

Figure 3.17: Distribution of events in the (a) delay plot and (b) rdelay parameter space, selected by using yield ratio to distinguish the electron recoil type from the nuclear recoil type.

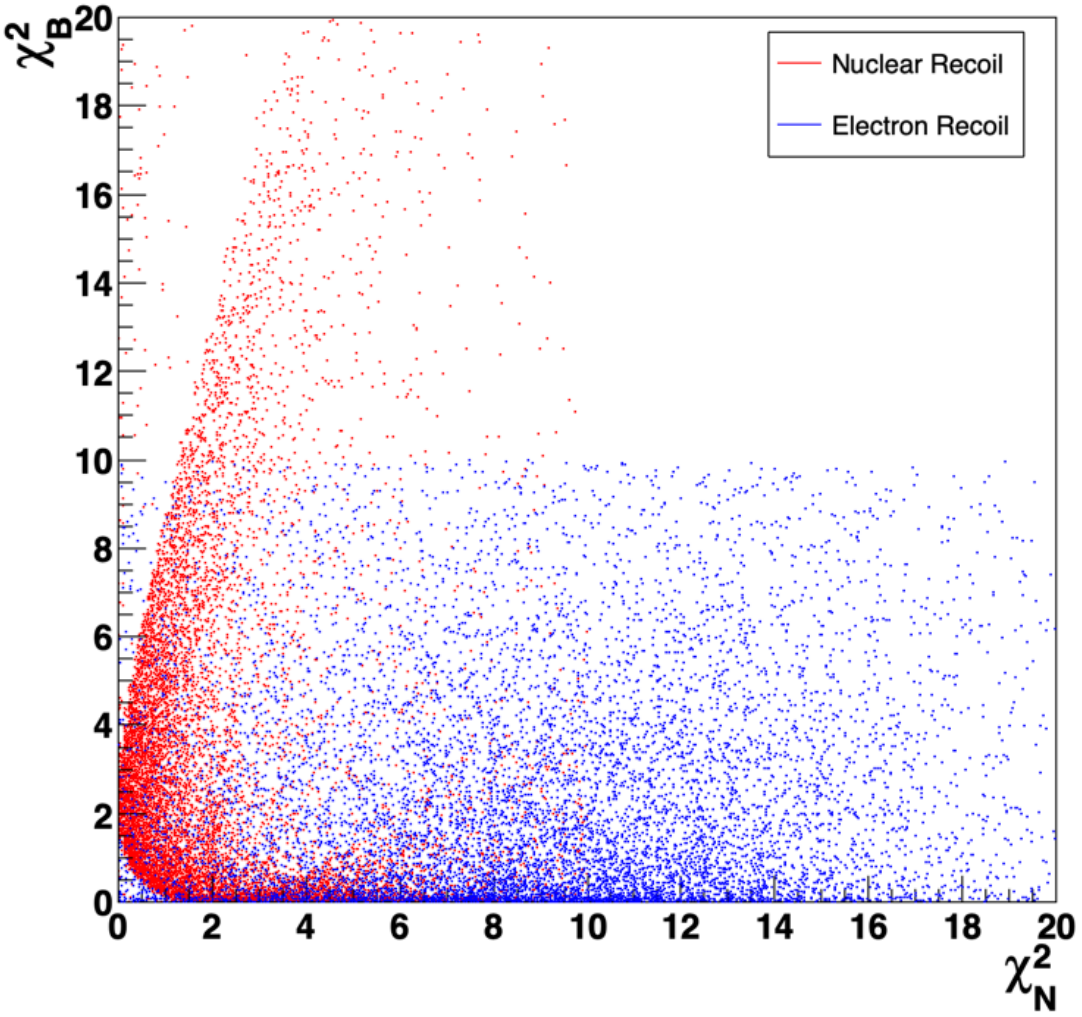

Figure 3.18: Likelihood analysis test to separate out nuclear and electron recoil events in the combined parameter space of χ^2_N and χ^2_B

4. THE MINER EXPERIMENT

4.1 Introduction

The Mitchell Institute Neutrino Experiment at Reactor (MINER) is a reactor based experiment proposed to pioneer the detection of Coherent Elastic Neutrino Nucleus Scattering(CEνNS) at a reactor, which is a major background for future low-recoil direct dark matter search experiments. CEνNS was first detected by the COHERENT experiment in CsI detectors using stopped pion beam at SNS [20, 21] and MINER aims to complement that observation using reactor neutrinos.

4.2 Experiment Location and Shielding

The MINER experiment is currently operating right next to a megawatt TRIGA (Training, Research, Isotopes, General Atomics) pool reactor at the Texas A&M Nuclear Science Center (NSC). This reactor facility has the advantage of a movable core and a thermal column cavity located in close proximity to the core where detectors can be deployed for the experiment. Though there is a natural overburden of 15 mwe(Meters Water Equivalent) on top of the cavity due to the reactor pool and the concrete walls, the background from sources like cosmic muons, surface radioactivity and the reactor background is expected to be challenging and the experiment has designed active and passive shielding to lower down the background level to $\sim$ 100 DRU (Differential Rate Unit).

The TRIGA reactor consist of 90 fuel elements which are enriched($\sim 20\%$) with ^{235}U core and operates at a nominal power of 1 MW (it operates at 900 kW to ensure fluctuations don't put them above MW). The reactor pool is made of high-density concrete wall to shield from high flux of neutron and gamma from the reactor. It has a thermal cavity in the same horizontal plane as the reactor core to do neutron irradiation where the MINER experiment is being setup.

The passive neutron shielding from the reactor core is achieved with commercial high-density polyethylene containers filled with water(water bricks) arranged in series of 18 inches of thick wall layers to form a total of 54 inches of water bricks between the core and the cavity. Two layers of lead gamma shield is placed surrounding the water brick layer closest to the detectors which help

to shield from gammas from the reactor core. The gamma-induced neutrons from the first lead layer is also shielded by this particular arrangement of layers. The experiment is housed inside a 6 in hermetic lead box to shield against any ambient core gammas. An initial lead shield close to the reactor in the pool is also added to reduce gammas which can leak through the existing shielding by large angle Compton scattering from the reactor pool wall. The various layers for the MINER experiment is shown in Figure 4.1

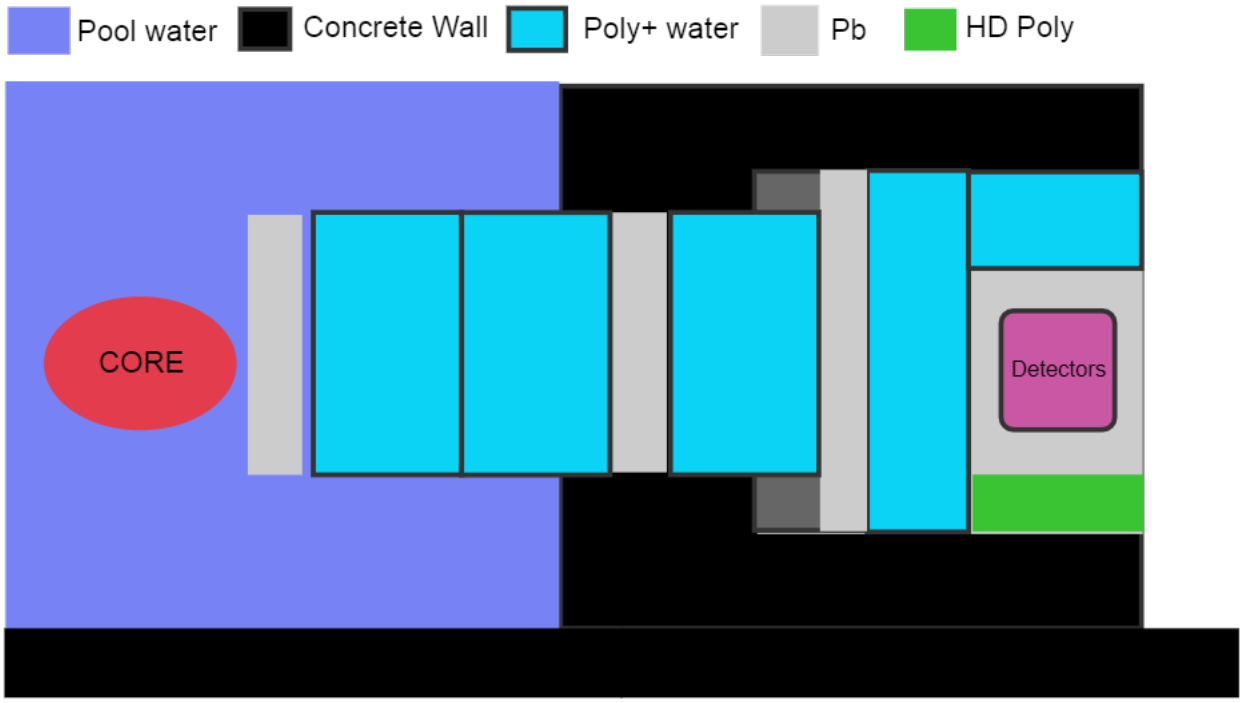

Figure 4.1: Schematic of the proposed shielding for the MINER setup. As seen, there is an initial layer of lead shield for gamma followed by multiple layers of water bricks for neutron shielding. The final layer is a Pb hermetic box to shield any ambient gammas. Background shielding due to cosmic muons is achieved with the concrete wall and reactor pool.

4.3 Cryogenics and related Electronics

The MINER experiment uses cryogenic semi-conductor detectors similar to SuperCDMS which are designed to operate at a temperature of 50 mK or lower. Though the experiment have completed its first run, I will discuss the setup and its preliminary results for the 2nd Run when the

hybrid detector is introduced in the experiment. The detectors are housed inside a cryogen-free BlueFors 400 μW refrigerator which provides the main cooling power. The fridge is surrounded by mu metal sheets to protect the cold electronics inside the fridge from external magnetic fields. In future runs, the cold volume of the refrigerator will be extended via a cold stem to place the detectors at the nearest distance of $\sim$ 2 m from the reactor core, similar to CDMS icebox design shown in Figure 4.2. The icebox will have concentric copper vessels(cans) which are thermally shielded by nested series of stages. Going from outside to inside, the cooling stages will be 4K stage, 50 K stage, 600 mK stage, 100 mK and mixing chamber. These copper cans also act as shield for alpha and beta particles.

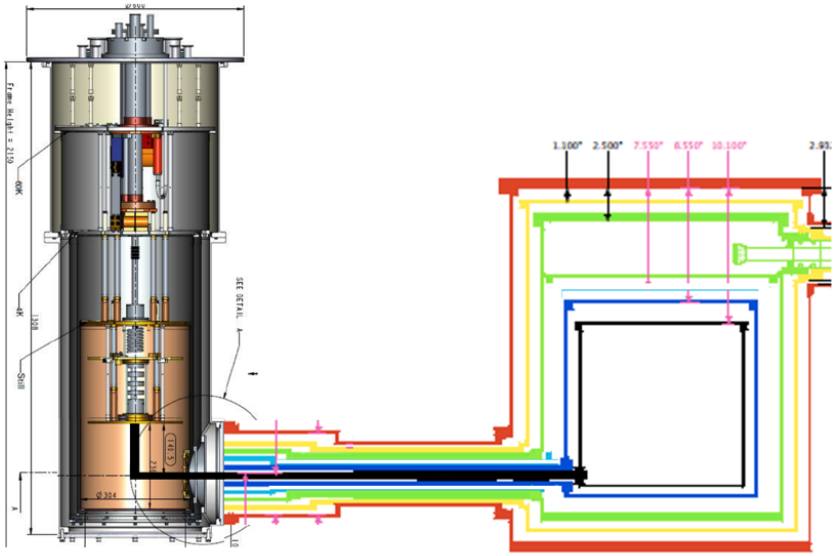

Figure 4.2: SuperCDMS Soudan Icebox design for reference only. MINER Icebox will follow a similar design.

The Run II (NSC Run 28) of MINER started operations in 2020 with one detector tower containing 1 hybrid detector and 1 Si HV detector. The detectors are housed inside Cu detector housings placed in a detector tower made of ultra-pure Cu, with the SiHV on top and the hybrid on the bottom of the arrangement. All five phonon channels of the hybrid detector and three inner channels of the SiHV detector (with a 3 in HV mask) are readout from the detector interface

boards(DIB) and connected to two SQUET cards (SQUID+FET, FET disabled in this case). Since each SQUET allows a maximum of 4 channels to readout at a time, the bottom four channels of hybrid is connected to one SQUET and the top channel of the hybrid along with the three channels of Si HV detector is connected to the other one.

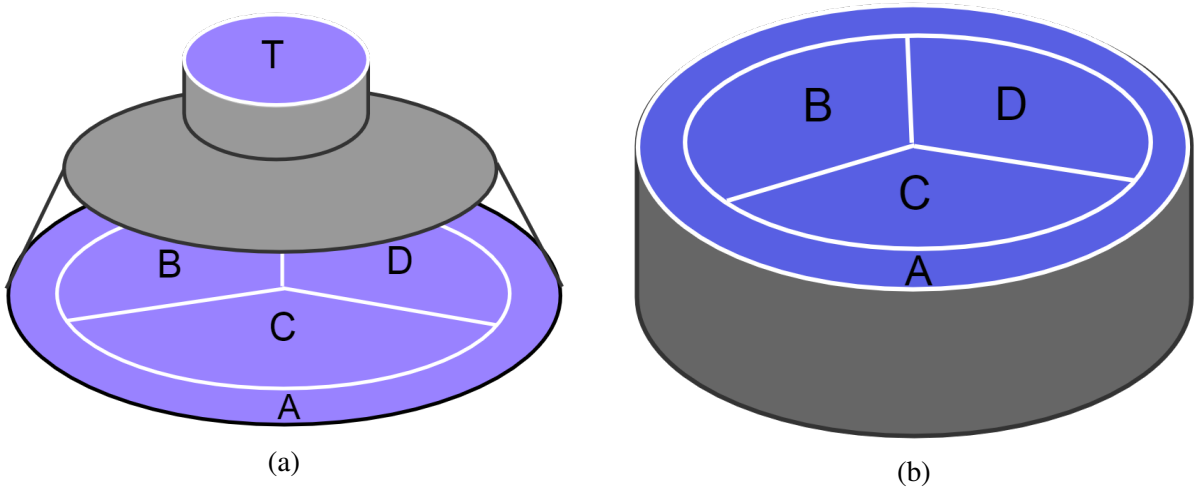

(a) (b)

Figure 4.3: The general shape of (a) hybrid and (b) Si HV detector with their channel layout.

The signal and control lines from each detector DIB are connected via a 50 wire cable to the Front End Board (FEB). This board has amplifiers and phonon readout circuits and its output is fed into a CAEN digitizer module. The FEB can also control the detector LEDs, biasing current in the SQUIDs, QET biasing etc. The FEB is operated with a Labview VI interface with a computer. The Receiver Trigger Filter (RTF) board is skipped in the warm electronics side using a very simple setup designed by the TAMU R&D Lab. Triggering (software trigger) is done through LabView VI designed to read and process the CAEN digitizer output. Two types of trigger is possible in this case: random triggering to collect unbiased data to monitor noise performance and threshold trigger to collect pulses above a certain threshold voltage.

4.4 Detectors and Experiment Setup for MINER Run II

As mentioned earlier, MINER Run II has two detectors: 1 Hybrid and 1 HV in the payload. The general layout of the detectors is illustrated in Figure 4.3. In the hybrid detector, the top side has one phonon channel (Channel T) and the bottom side has four phonon channels arranged as shown in Figure 4.3. All channels are being readout in this run and are connected to the biasing circuits. The bottom channels are kept at a voltage V_2 potential and top channel is externally biased to a voltage of V_1 to have a detector bias of $(V_2 - V_1)/2$. In the silicon HV detector, one side has four phonon channels and only the inner three channels are readout while the other channel is at floating potential while the other side is used to provide voltage biasing in contact-free mode.

The hybrid crystal thickness is 1 inches with a radius of 3 inches and weigh about 112 gm. The HV crystal thickness is approximately 1 cm with a radius of 3 inches and weigh about 100 gm. For both the detectors, the crystal axis [1 0 0] is oriented to point in the z direction. The fabricated crystals are held by copper housing which is the supporting structure for these crystals and their digital interface board(DIB) which connects the detector channels to the readout boards via wirebonds. Only Si substrates are used in this run and the complete tower has these two detectors only.

An ^{241}Am source is kept facing Channel D on the hybrid detector and an ^{55}Fe source is kept at the center of the Si HV detector. The 60 keV events from the ^{241}Am source on the top and bottom region of the hybrid is used to calibrate the phonon channels of the detector. There are two external radioactive sources available: ^{57}Co for electron recoil calibrations and ^{252}Cf for neutron recoil calibrations. As shown in Figure , the fridge housing the detector towers is surrounded with a 4 inch Pb wall and the fridge was about 2 m away from the thermal column where the icebox will be mounted in future runs.

4.5 Data Analysis of MINER Run II

The data analyzed here are collected over two weeks, in July-August 2020, using the detectors mentioned in the previous section. Multiple datasets are taken with varying run duration with

LED flashing in between runs to determine an optimum operation procedure. LED flashing helps to equilibrate the charge population which is built up in the detectors, especially in contact-free mode. The general procedure to do led flashing involves keeping the detectors in ground potential and flashing the led lights for 4-5 times manually, following which the high voltage is applied immediately and data recording in resumed. Data quality and data selection criteria is similar to previous analysis discussed in the last chapter. We will be focusing the analysis from the hybrid detector in the following sections.

4.5.1 Noise Performance

Noise traces are recorded at the beginning of each dataset in random triggering mode of the DAQ VI. These are 10k sample traces which are split into 2k traces to be used as template for the OF algorithm. Figure 4.4 shows the noise level and high frequency noise spectrum in the current location of the detectors as seen by the hybrid detector. The noise level is comparable to the Texas A& M facility environment that we have seen in the previous chapter.

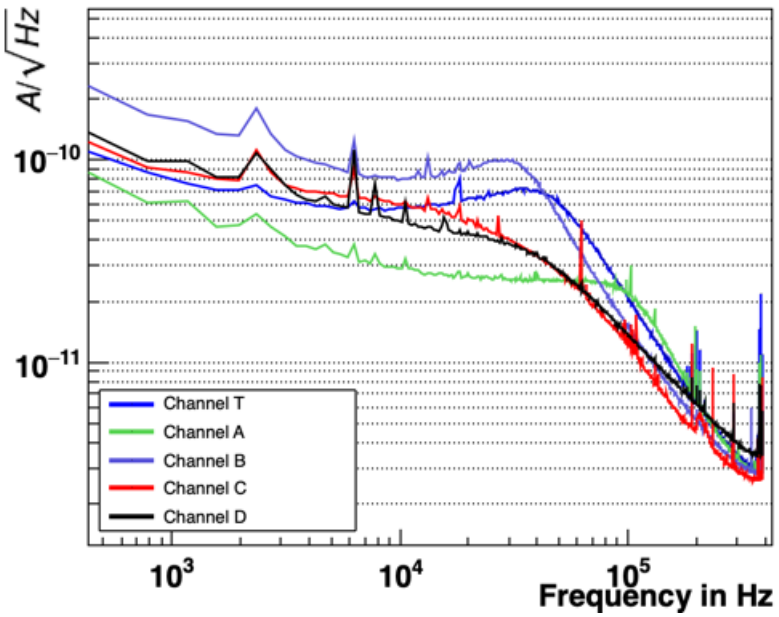

Figure 4.4: NoisePSD for all channels of the hybrid detector at a detector bias voltage of 0V in MINER Run II

4.5.2 Phonon Baseline Resolution

To calculate phonon baseline resolution, the spectrum of ^{241}Am internal source on the two sides of the hybrid detector is plotted at different voltages and fitted with a Gaussian function. The fitted gaussian mean is used to scale the OF fitted noise amplitude spectrum as shown in Figure 4.5. The phonon baseline resolution on the top and bottom side of the hybrid is measured to be 74 eV and 242 eV at 0V respectively. The increase in the phonon baseline for the hybrid detector from earlier measurement can be attributed to factors like environmental noise in the facility, QET tuning parameters etc. The resolution improves at higher voltages, but is limited by the saturation of the 60 keV on the top phonon mask.

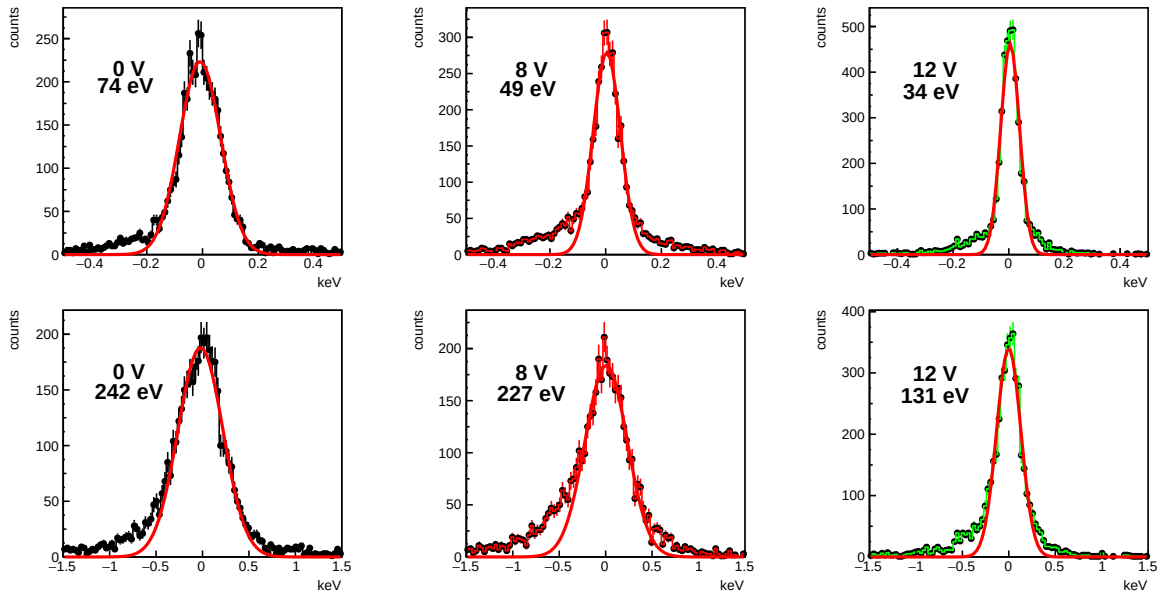

Figure 4.5: Phonon baseline resolution measurements at different voltages for the top (first row) and bottom side (second row) of the hybrid detector. The baseline resolution improves at higher voltages as expected.

4.5.3 Reactor background monitoring

One of the main reasons to include the hybrid detector in the MINER experiment is the background monitoring capability of the detector and to have a quantitative estimation of the gamma

and neutron flux from the reactor in the detector setup. Multiple hours of data with the reactor "on" is taken and compared with hours when the reactor is "off". As in Figure 4.6, the background count rate increases for reactor "on" as compared to "off" data, seen by the hybrid detector.

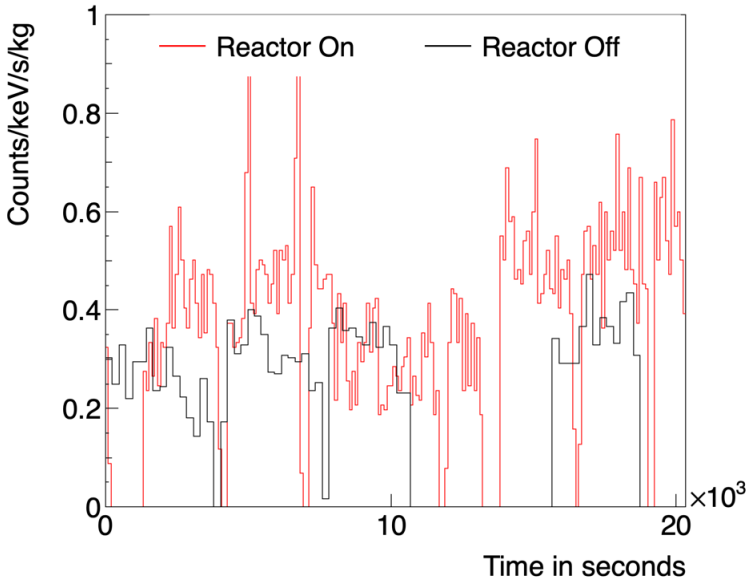

Figure 4.6: Count Rate of all events in the energy range 1-10 keV as a function of time duration of run for the reactor on and off datasets

The trigger conditions for the dataset is modified to only include events triggered by the channels with no internal sources directly on them. Also, the energy range for counts is chosen such that no internal lines from the internal sources are present in that energy region. Figure 4.7 shows the yield plot with the previously defined electron and nuclear recoil 1 σ bands for the energy range 20-45 keV. The raw counts of background electron and nuclear recoil events for the reactor core on and off is measured to be ~ 350 DRU and ~ 240 DRU respectively, with a minimal shielding of 4" Pb bricks in an open-top box design setup. In future runs, the full MINER shielding as discussed in Section 4.2 will be used.

It is to be noted that the other detector, Si HV didn't see any significant change in the event rate for the two datasets. Since this estimation of background trigger rate is highly dependent on the

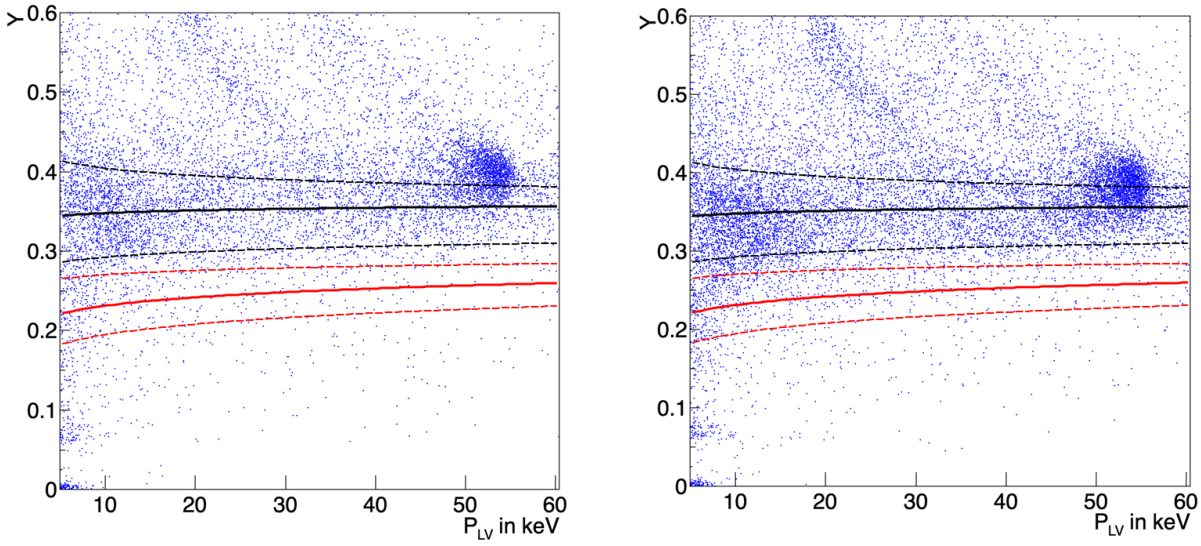

(a) 5 hour dataset with reactor core ON

(b) 11 hour dataset with reactor core OFF

Figure 4.7: Hybrid yield plot showing the electron recoil recoil and nuclear recoil events in the (a) reactor on and (b) reactor off datasets. The raw counts are calculated from this yield plot. Nuclear Recoil background without single scatter cut is estimated to be $\sim$ 20 DRU

trigger rate of the digitizer used for the setup, future runs will be done in binary data format which is found to have a higher trigger rate for this particular DAQ setup.

4.6 Energy threshold for MINER Run II

An extended dataset over a week is done in the presence of the external radioactive source ^{252}Cf to have a high statistics electron and nuclear band definition with the hybrid detector and the corresponding energy threshold for this run is estimated from this plot to be $\sim$ 3 keV, as shown in Figure 4.8. In comparison to the yield plot from hybrid in the last chapter, this run doesnot have the 6 keV line in the lower energy range. In the high statistics setup, the neutron band seem to loose count rate at energies close to the trigger threshold of the run. Since the dataset is taken with trigger conditions: the top channel and one of the bottom inner channel (labelled as Channel D) trigger in an OR logic, it is expected that the trigger rate will decrease for lower energy recoil in the bands due to decrease in the number of electron-hole pairs production in low energy interactions as well as Lindhard suppression. The neutron statistics has further decreased by 4-fold since we

are triggering only on one of the four bottom phonon channels which might have lead to a sharp decline in the count rate close to the trigger threshold.

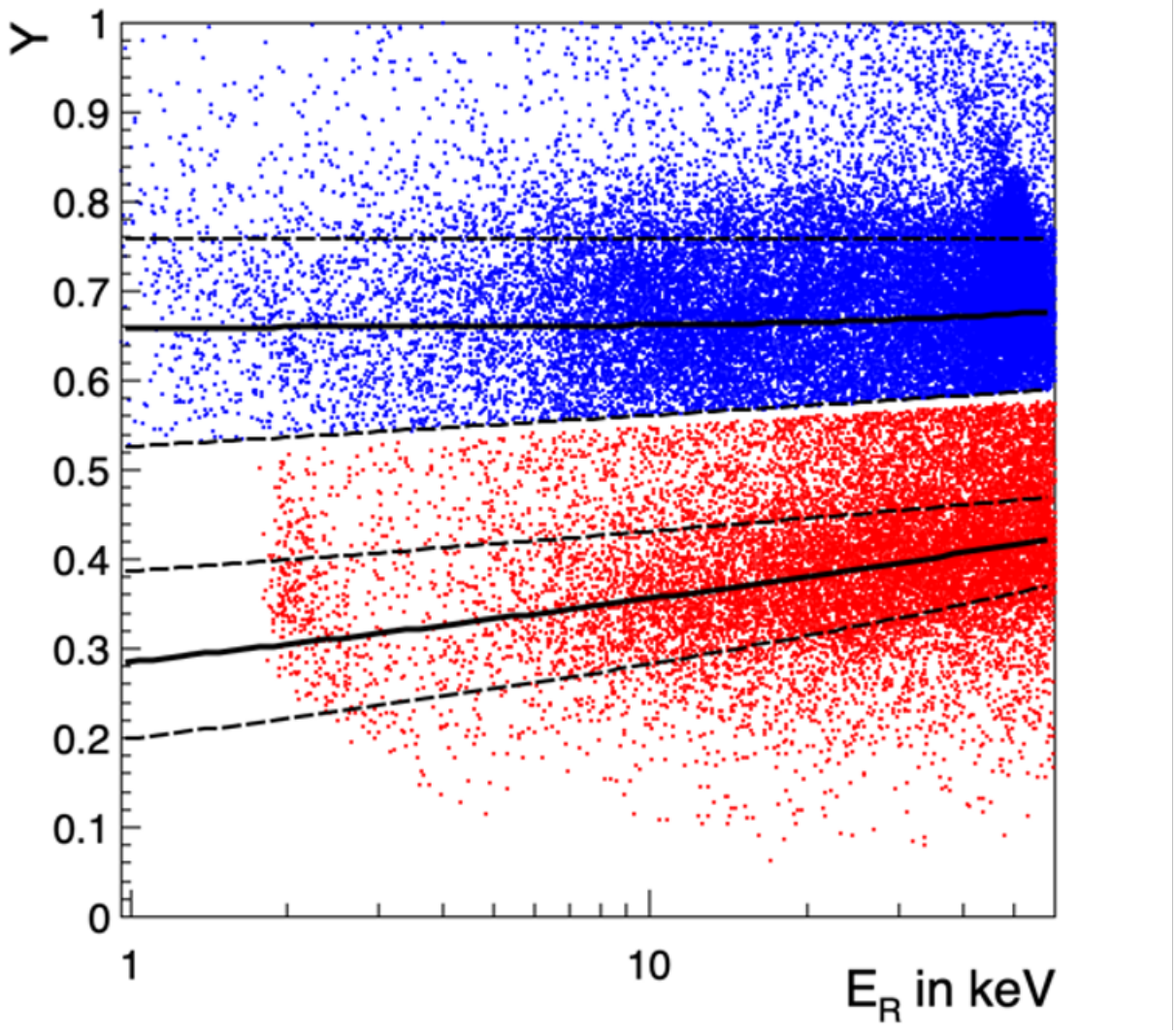

Figure 4.8: Yield plot showing the electron (blue) and nuclear (red) recoil events in presence of an external neutron source ^{252}Cf

Figure 4.9 shows the trigger rate of each population of neutrons (from low energy neutrons to higher energy neutrons) labelled by colors on the yield plot. The corresponding number of triggers

from the two triggering phonon channels are also shown in the figure. The center plot (colored in black) is the noise population near the threshold of the experiment.

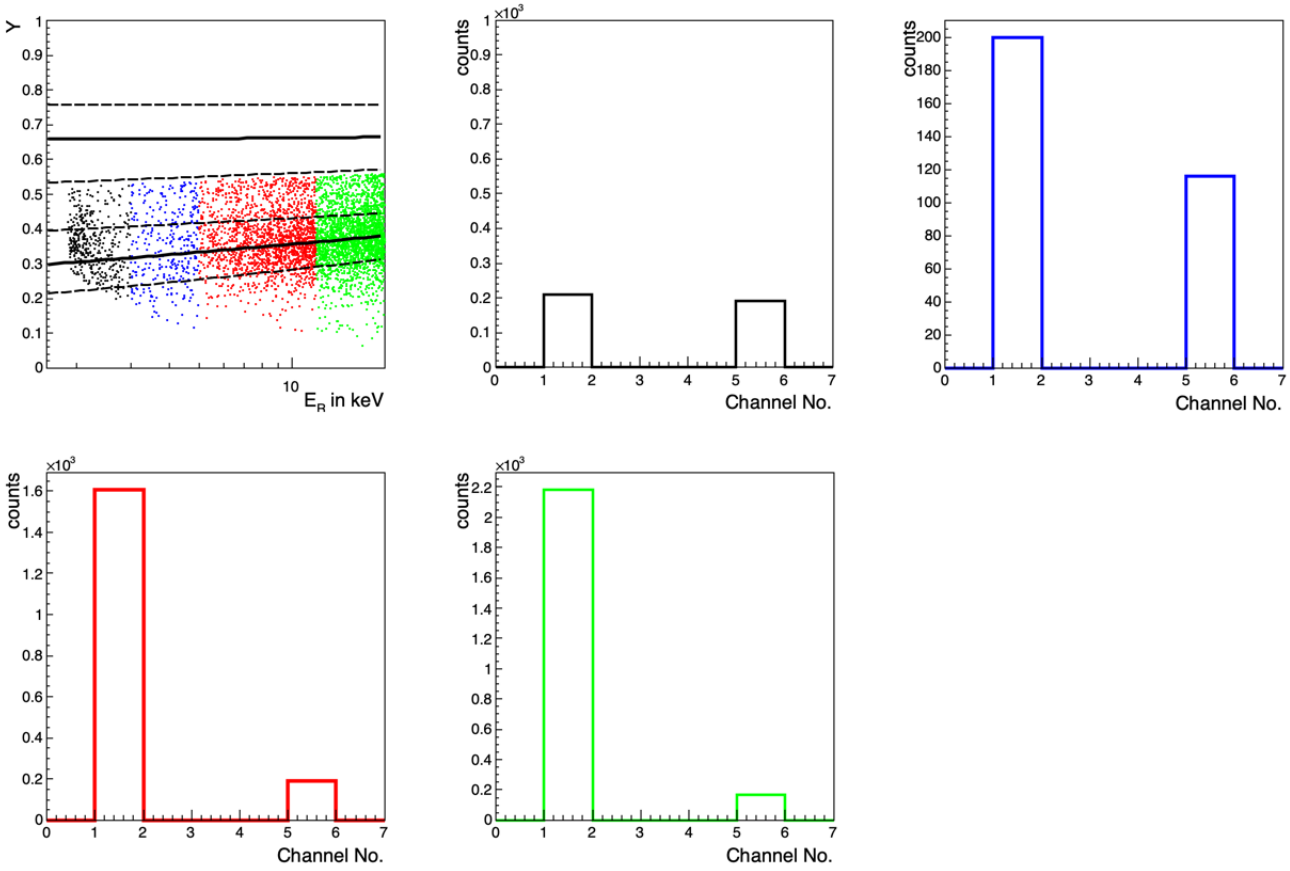

Figure 4.9: Plot showing the yield plot of ^{252}Cf neutron events with colored event population for neutrons of different energy range and their corresponding trigger count rate in the two triggering phonon channels. Here Channel 1 is the top phonon channel and Channel 5 is the bottom phonon channel labelled as D.

4.7 Future Run Plans and Outlook

While the second run of MINER demonstrated the state of the art technology available in the experiment, it also allowed to identify areas to improve. I will listing the different improvements that have been proposed and going to be implemented for the next run.

4.7.1 DAQ Trigger Rate Improvements

As noted earlier, the background rate estimation and overall trigger rate for data acquisition is highly dependent on the DAQ hardware used in the experiment. Currently, data is being recorded and stored by a CAEN 8 channel 14 bit digitizer with a recoding rate of 100 MS/s. During data taking, it was found that the DAQ system is unable to keep up the recording speed(with a recording event rate of $\sim 20 - 30$ Hz) with the current labview VI and readout filetype . One solution to this problem is to record the data in binary format which seem to increase the performance of the labview VI used for the data recording process. The next run is set to use binary data format for recording and the analysis scripts are modified accordingly.

4.7.2 Threshold reduction via trigger-less DAQ

The energy spectrum of WIMP is exponential with no features and one can benefit from using lower energy thresholds in this scenario. In MINER Run II, the recoil energy threshold was $\sim 2-3$ keV_{ee} which is very impressive, but the baseline resolution of 250 eV_{ee} for the hybrid detector (and ~ 18 e-h pair equivalent for SiHV detector) indicates that there is scope for improvement. Low frequency noise make noise triggers in the 10 kHz frequency range and a reduction in this noise would allow for a significantly lower energy threshold in the experiment. This will be possible with a trigger-less DAQ system where the continuous stream of data is recorded as long traces without any trigger-threshold conditions in the DAQ system. The event pulses from those traces can be filtered out offline with analysis algorithm techniques which will significantly help tp reduce low-frequency noise.

4.7.3 Fiducialization

In the MINER Run II analysis, there were no cuts to remove surface recoil events from the bulk events. Since the events near the surface has various systematics like charge trapping and reduced Luke amplification, the outer ring phonon channel for both the detectors need to be read to better define a fiducialization which will be undertaken in the next run.

4.7.4 Future MINER runs

As a pioneer experiment to try to detect CEνNS neutrinos at a reactor, MINER Runs are being planned with more and more detectors which will increase the total mass of active detection volume, currently estimated to be $\sim$ 2kg which in turn, will increase the total exposure of the experiment. Further improvements in SQUID biasing monitoring and DAQ system will lead to improvements to handle higher trigger rate (useful for calibration studies) for better statistics at low energy region. With the full shielding around the current fridge setup, a reduced total background event rate is expected.

Since future dark matter detectors will reach the neutrino floor, the study of CEνNS neutrinos is very fundamental and a major scientific accomplishment in itself. We hope to detect CEνNS neutrinos at the reactor in the near runs of this experiment.

5. SUMMARY AND OUTLOOK

5.1 Summary

This thesis described a novel detector design which relies purely on phonon signals to discriminate between electron recoil and nuclear recoil events. Since ionization signal uses FET amplifiers which has been a major source of noise in the low threshold dark matter experiments, this detector has the potential to reach $\sim$eV threshold mainly due to use of SQUID amplifiers which traditionally have very low intrinsic noise. With the ability to measure athermal primary phonons and luke phonons separately, we demonstrated the first prototype of the hybrid detector with minimal design complexity. We reached a baseline resolution of 34 eV from the top phonon sensors of the hybrid and 234 eV from the bottom phonon channels at a voltage bias of 0V. The maximum operable detector bias voltage of 18V (baseline top: 17 eV and bottom: 101 eV) is chosen based on current hardware design of the electronics circuit which limits us to reach our ultimate goal of single electron sensitivity. I will conclude this thesis with discussions on the future possible improvements to the hybrid detector which will truly help us to reach the ultimate detection capability from this technology.

5.2 Future Improvements

5.2.1 Field Shaping Electrodes

The current hybrid detector setup doesnot have dedicated field shapers to guide the electric field inside the detector to help increase the transmission of the charges through the neck area of the detector. One possible field shaper is shown in Figure 5.1, where one or more grounded aluminum rings can be placed close to the neck which will alter the electric field lines to avoid ending up on the surfaces of the detector. This will help reduce surface recoil events in the detector and will help to define a better fiducial volume.

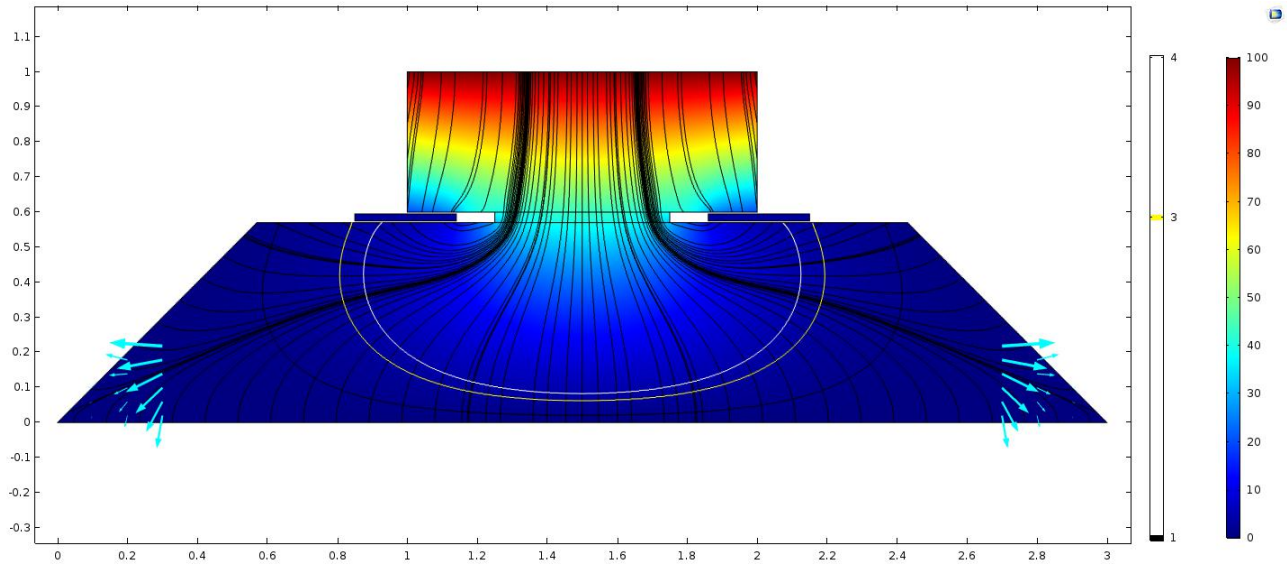

Figure 5.1: Simulated electric field inside the conical hybrid detector in presence of an aluminum field shaper near the neck region. The arrows indicate the dead area of the detector which has electric field < 0.5 V/cm. Both the axes are in inches and the color scale is in volts.

5.2.2 Biasing Electronics

The current analysis with the hybrid detector is limited to 12V detector bias mainly due limitation from the CDMS electronics circuit. The SQUET board containing the SQUIDs and FETs has grounded electrical lines instrumented in proximity with the circuit used to bias the QETs. Since this particular detector is voltage biased through the same circuit which bias the QETs of the phonon channel as well, the current run of the detector is kept limited to ± 20 V on any of the voltage lines shown in Figure 1.6. Further modifications to the electronics circuit will leverage the detector bias capabilities of the hybrid detector. As apparent from Figure 3.12, higher detector bias voltage is preferable to reach lower phonon baseline resolutions and hence to do low mass dark matter search.

5.2.3 Detector Geometry

The formalism of the hybrid detector technology is independent of the detector design and only depends on the efficient transport of charges between the two regions of the detector. The conical design described in this thesis is the minimalist design strategy to demonstrate the power

of the technology and its viability. Multiple variations of the hybrid detector is possible which will leverage the capability of the detector in the transport of charges. One variation which is possible is shown in Figure 5.2, which is a bell-shaped hybrid detector design. The advantage of this design is that the detector geometry is aligned closely with the electric field lines inside the detector which will reduce trapping of charges at the sidewalls or the neck area. One limiting factor

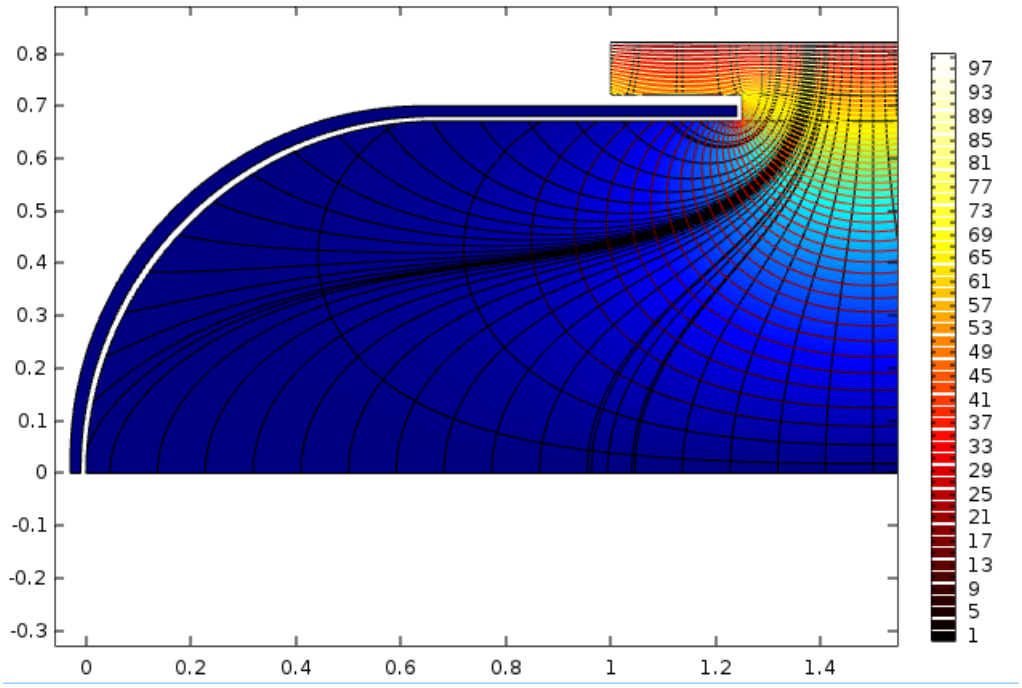

Figure 5.2: Simulated bell-shaped hybrid detector with field shaper showing the electric field lines in black color and electric field gradient contours for a biased voltage of 100 V. Both the axes are in inches and the color scale is in volts.

of this geometry is that it will require advance fabrication steps to create a bell-shape structure on a cylindrical silicon crystal.

5.3 Sensitivity Projections

Figure 5.3 shows the projected limits with the hybrid detector using optimal interval method with a background spectra obtained from SuperCDMS-SNOLAB background estimates [22]. Assuming standard halo model and spin-independent interactions of dark matter with silicon nu-

clei, the dark matter spectrum is calculated to determine a 90% Confidence Limit exclusion cross-section of WIMP-nucleon interactions for a relevent dark matter mass range.

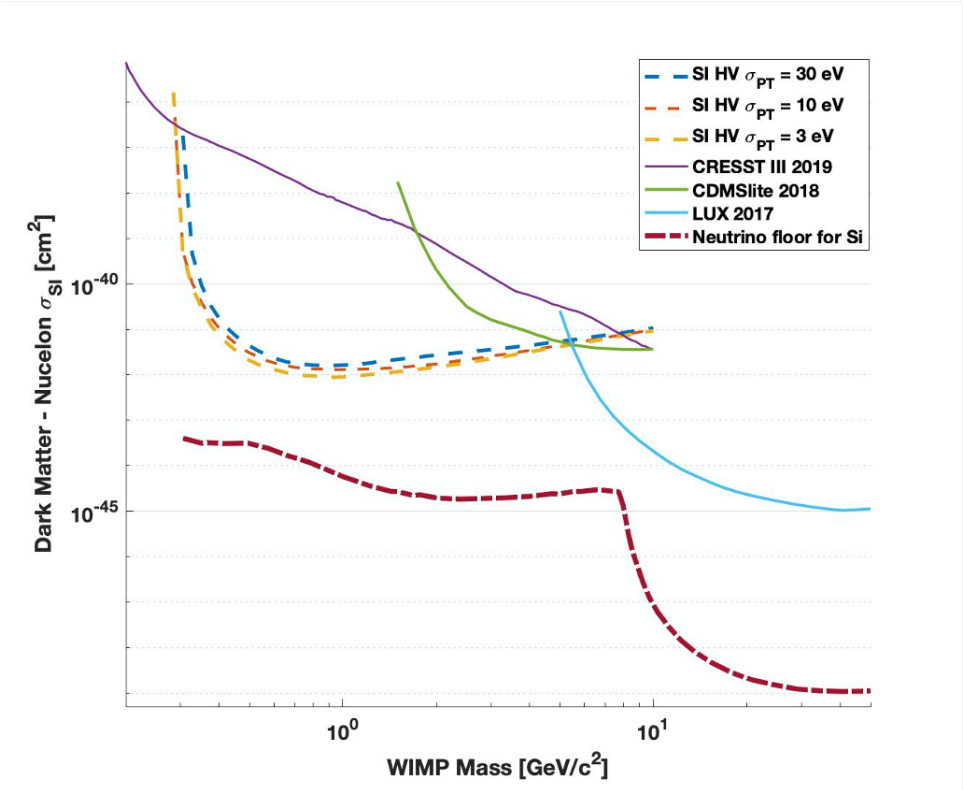

Figure 5.3: Projected limit for the hybrid detector (approximated as a HV detector of mass 100 g with 30 eV baseline resolution) for a run in the SuperCDMS-SNOLAB experiment with a year-long exposure time. Three different baseline resolution projections are shown and compared with published results from other competitive experiments.

This prototype hybrid detector performance has established the ground work for future improvements on the hybrid detector theory and opened up new possibilities on hybrid-style detectors with new materials. All dark matter experiments will ultimately reach the neutrino floor and we hope to detect dark matter till then.

REFERENCES

[1] P. A. R. Ade *et al.*, "Planck 2013 results. XVI. Cosmological parameters," *Astron. Astrophys.*, vol. 571, p. A16, 2014.

[2] "Planck's new cosmic recipe." Web: http://sci.esa.int/planck/51557-planck-new-cosmic-recipe/.

[3] P. A. R. Ade *et al.*, "Planck 2013 results. I. Overview of products and scientific results," *Astron. Astrophys.*, vol. 571, p. A1, 2014.

[4] Y. Sofue and V. Rubin, "Rotation curves of spiral galaxies," *Annual Review of Astronomy and Astrophysics*, vol. 39, no. 1, pp. 137–174, 2001.

[5] D. C. Moore, *A Search for Low-Mass Dark Matter with the Cryogenic Dark Matter Search and the Development of Highly Multiplexed Phonon-Mediated Particle Detectors*. PhD thesis, Caltech, 2012.

[6] R. Basu Thakur, *The Cryogenic Dark Matter Search low ionization-threshold experiment*. PhD thesis, Illinois U., Urbana, 2015.

[7] L. Anderson, Aubourg, *et al.*, "The clustering of galaxies in the SDSS-III Baryon Oscillation Spectroscopic Survey: baryon acoustic oscillations in the Data Releases 10 and 11 Galaxy samples," *Monthly Notices of the Royal Astronomical Society*, vol. 441, pp. 24–62, 04 2014.

[8] G. Bertone, D. Hooper, and J. Silk, "Particle dark matter: Evidence, candidates and constraints," *Phys. Rept.*, vol. 405, pp. 279–390, 2005.

[9] S. P. Martin, "A Supersymmetry primer," *Adv. Ser. Direct. High Energy Phys.*, vol. 18, pp. 1–98, 1998.

[10] J. Silk *et al.*, *Particle Dark Matter: Observations, Models and Searches*. Cambridge: Cambridge Univ. Press, 2010.

[11] J. D. Lewin and P. F. Smith, "Review of mathematics, numerical factors, and corrections for dark matter experiments based on elastic nuclear recoil," *Astropart. Phys.*, vol. 6, pp. 87–112, 1996.

[12] S. A. Hertel, "Advancing the Search for Dark Matter: from CDMS II to SuperCDMS," *Massachusetts Institute of Technology*, 2012.

[13] P. N. Luke, J. Beeman, F. S. Goulding, S. E. Labov, and E. H. Silver, "Calorimetric ionization detector," *Nucl. Instrum. Meth. A*, vol. 289, pp. 406–409, 1990.

[14] B. S. Neganov and V. N. Trofimov, "Colorimetric method measuring ionizing radiation," *Otkryt. Izobret.*, vol. 146, p. 215, 1985.

[15] M. C. Pyle, *Optimizing the design and analysis of cryogenic semiconductor dark matter detectors for maximum sensitivity*. PhD thesis, Stanford U., 2012.

[16] A. J. Anderson, *A Search for Light Weakly-Interacting Massive Particles with SuperCDMS and Applications to Neutrino Physics*. PhD thesis, MIT, 2015.

[17] Z. Ahmed *et al.*, "Results from a Low-Energy Analysis of the CDMS II Germanium Data," *Phys. Rev. Lett.*, vol. 106, p. 131302, 2011.

[18] A. Jastram, *CDMS Detector Fabrication Improvements and Low Energy Nuclear Recoil Measurements in Germanium*. PhD thesis, Texas A-M, 2015.

[19] J. P. Filippini, *A Search for WIMP Dark Matter Using the First Five-Tower Run of the Cryogenic Dark Matter Search*. PhD thesis, UC, Berkeley, 2008.

[20] D. Akimov *et al.*, "Observation of coherent elastic neutrino-nucleus scattering," *Science*, vol. 357, p. 1123–1126, Aug 2017.

[21] D. Akimov *et al.*, "COHERENT Collaboration data release from the first observation of coherent elastic neutrino-nucleus scattering," 4 2018.

[22] R. Agnese *et al.*, "Projected Sensitivity of the SuperCDMS SNOLAB experiment," *Phys. Rev. D*, vol. 95, no. 8, p. 082002, 2017.

APPENDIX A

LIKELIHOOD RATIO TEST

The Likelihood Ratio test helps to efficiently merge multiple observations in form of parameters into a single decision making criteria. This section will describe the method used to find the likelihood ratio test to separate out the electron recoil events from the nuclear recoil events from the data obtained with the hybrid detector.

A.1 χ^2 definition

Let us assume the likelihood function to be a multivariate gaussian distribution of the form

$$L(x) = (2\pi det|C|)^{-N/2} e^{-\frac{1}{2}(x-\mu)^T C^{-1}(x-\mu)} \tag{A.1}$$

where μ is a 3-dimensional vector of the parameters: $rdelay$, P_{HV} and P_{LV} and C is a 3x3 covariance matrix of the distribution:

$$C_{ij} =< x_i x_j > - < x_i >< x_j > \tag{A.2}$$

In the gaussian approximation, the form of the likelihood ratio test will take the logarithmic form

$$logL(x) = -N/2(\log 2\pi + \log det|C|) - \frac{1}{2}(x-\mu)^T C^{-1}(x-\mu) \tag{A.3}$$

Defining the above formula for the signal events as $L_{sig}(x_0)$ and background events as $L_{bkg}(x_0)$, we can define the ratio test as

$$\begin{aligned} & logL_{sig}(x_0) - logL_{bkg}(x_0) > logc \\ =>& \frac{N}{2} log \frac{det|C_{bkg}|}{det|C_{sig}|} + \frac{1}{2}(\chi^2_{bkg} - \chi^2_{sig}) > c \end{aligned} \tag{A.4}$$

where χ^2 is energy-dependent and is defined as

$$\chi^2 = (x - \mu(E))^T C^{-1}(E)(x - \mu(E)) + Nlogdet|C(E)| \tag{A.5}$$

This expression of χ^2 is valid if there is no dependence of the likelihood functions on energy E beyond the mean and covariance matrix.

A.2 Application to Hybrid Data

A.2.1 Event Samples

The electron recoil and nuclear recoil event populations were characterized using the functional form of the fitted bands in the yield plot of the data taken with ^{252}Cf source. All events within 1σ of the electron recoil band is used as electron recoil events and within 1σ of the nuclear recoil band as nuclear recoil events for the analysis. All events were chosen to pass the standard quality cut of "maxtail" as used during the analysis.

A.2.2 Parameter distribution and fitting

The three dimensional parameter space defined by rdel(radial delay of phonons relative to trigger time), P_{HV}(phonon amplitude of pulse in the top side of the hybrid using integral method) and P_{LV}(phonon amplitude of pulse in the bottom side of the hybrid using integral method) is constructed as a function of energy, shown in Figure A.1. It is seen that the variances of the parameters increases at low energies. The mean $\mu_{b/n}$ of each distribution is calculated using a Gaussian approximation to the distribution and taken to be constant with energy for simplicity. The nuclear recoil distribution is divided into bins in recoil energy: [3-6, 6-14, 14-18, 18-26, 26-38 and 38-48] keV. Similarly, the electron recoil distribution is divided into bins: [20-22, 22-24, 24-26, 26-30, 30-35 and 35-40] keV to avoid regions with lines from the internal sources .In each bin, the covariance matrix is calculated with respect to the fitted mean value and a least-square fitting of the form $\sigma^2(E) = a + b/E^2$ is done for the variances. The correlations are taken to be constant with energy. The different fitted distributions are shown in Figure A.2 and the fitted

functions are the black curves in the figure.

A.2.3 χ^2 parameter for signal and background

With the fitted parameters, the signal χ^2_N and background χ^2_B distributions are calculated using Equation A.5 and shown in Figure 3.18. It is apparent that the fraction of neutron events passing the cut of the form $\chi^2_N < 10$ shows less variation as a function of energy.

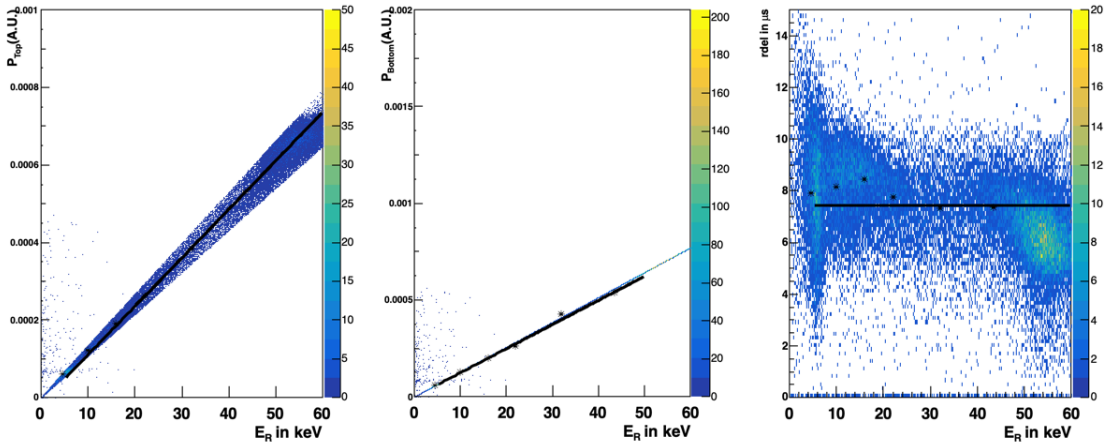

(a)

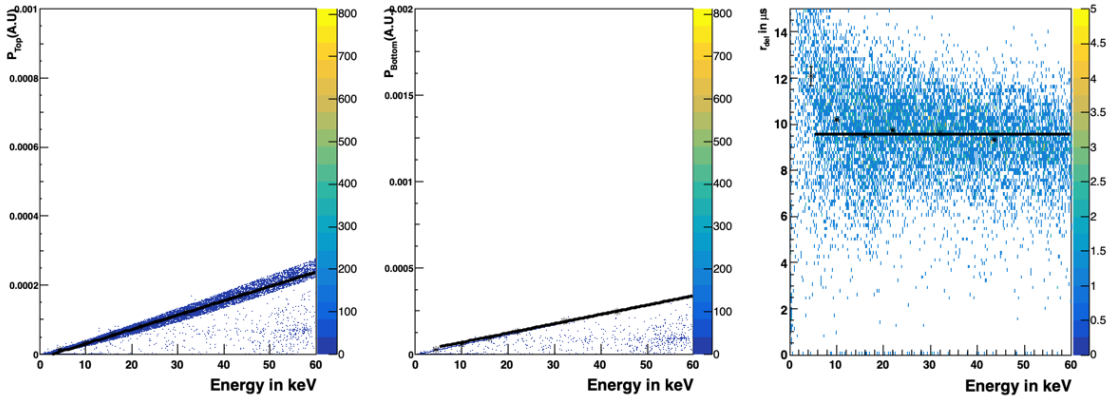

(b)

Figure A.1: Mean of the ER and NR distributions for the three parameters considered in the analysis. (a) shows the distribution of $P_{HV/Top}$, $P_{LV,Bottom}$ and $rdel$ parameters in the sample of electron recoil (ER) events. (b) shows the distribution of the same three parameters for nuclear recoil (NR) events. A black line is drawn to show the fitted mean used for the calculation. A linear behavior of the parameters is found for the given energy range.

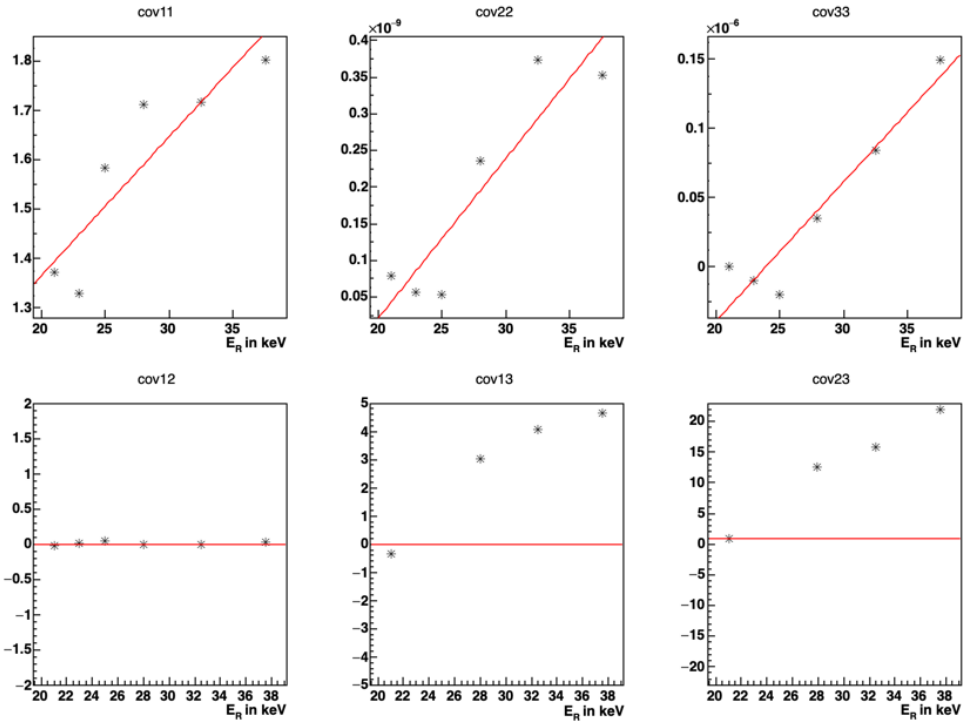

(a)

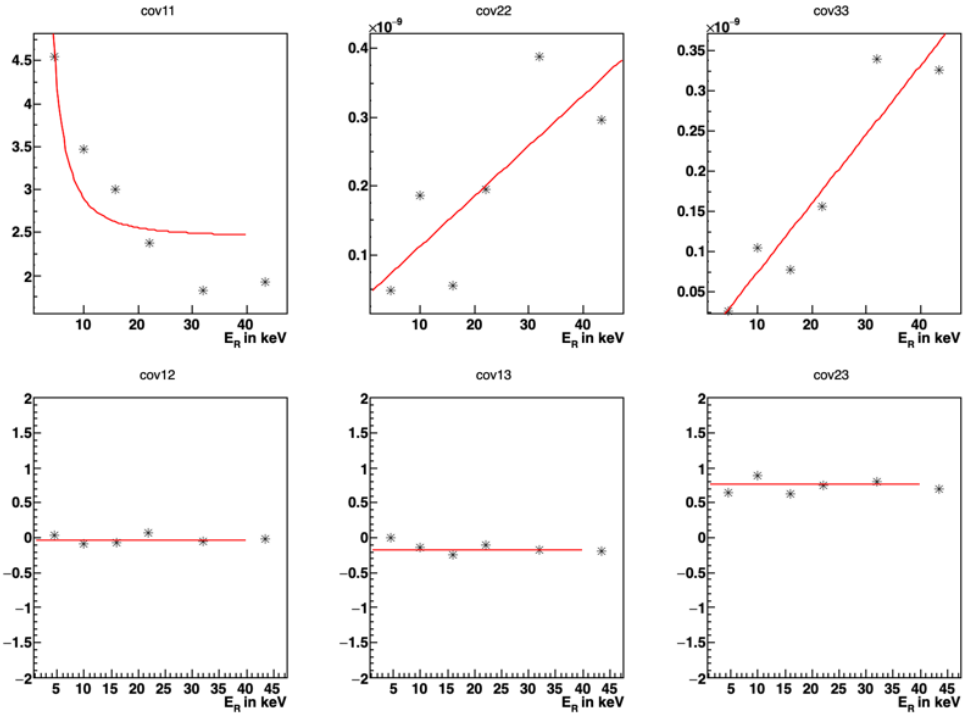

(b)

Figure A.2: Covariance matrix elements for the ER and NR events. The red line indicates the estimated mean for the calculation.